

Late-afterglow Emission from a Quasi-spherical Outflow in a stratified environment

N. Fraija,¹ B. Betancourt Kamenetskaia,² A. Galván,³ A. Montalvo,¹ A. C. Caligula Do E. S. Pedreira,¹ P. Veres,⁴ R. L. Becerra,⁵ M.G. Dainotti,^{6,7} S. Dichiara,⁸ H. León Vargas³

¹*Instituto de Astronomía, Universidad Nacional Autónoma de México, A. P. 70-264, Cd. Universitaria, Ciudad de México, México*

²*Cosmology, Gravity, and Astroparticle Physics Group, Center for Theoretical Physics of the Universe, Institute for Basic Science (IBS), Daejeon, 34126, Korea*

³*Instituto de Física, Universidad Nacional Autónoma de México, Apdo. Postal 70-264, Cd. Universitaria, Ciudad de México 04510*

⁴*Center for Space Plasma and Aeronomics Research (CSPAR), University of Alabama in Huntsville, Huntsville, AL 35899, USA*

⁵*Department of Physics, University of Rome - Tor Vergata, via della Ricerca Scientifica 1, 00100 Rome, IT*

⁶*Division of Science, National Astronomical Observatory of Japan, 2-21-1 Osawa, Mitaka, Tokyo 181-8588, Japan*

⁷*The Graduate University for Advanced Studies (SOKENDAI), 2-21-1 Osawa, Mitaka, Tokyo 181-8588, Japan*

⁸*Department of Astronomy and Astrophysics, The Pennsylvania State University, 525 Davey Lab, University Park, PA 16802, USA*

Accepted XXX. Received YYY; in original form ZZZ

ABSTRACT

Gamma-ray bursts (GRBs) are cosmic events occurring at large distances beyond our galaxy. They provide a unique opportunity to study electromagnetic patterns not seen elsewhere. When the collimated GRB outflow interacts with the outer layers of a star or the wind generated by a binary neutron star merger, it releases energy, forming a quasi-spherical outflow around it. This broad outflow begins to radiate once it has transferred enough energy to the surrounding medium. We have developed a new analytical model that describes the synchrotron afterglow scenario of the quasi-spherical outflow, including factors such as stratified density, self-absorption regime, and the fraction of electrons accelerated by the shock front. We also successfully describe the multiwavelength observations of a sample of IGRB afterglows (GRB 980425, 031203, 060218, 100316D, 130603B, 150101B and 171205A) that exhibited a late component, analyzed in both stellar wind and constant-density environments. Our analysis shows that a constant-density environment is favored. Additionally, we consider the multiwavelength upper limits of the short bursts reported in the Swift-BAT database.

Key words: Acceleration of particles – radiation mechanism: non-thermal – gamma-rays bursts: individual: (GRB 980425, 031203, 060218, 100316D, 130603B, 150101B and 171205A)

1 INTRODUCTION

The most luminous events in the Universe are gamma-ray bursts (GRBs), which are created when massive stars collapse (Woosley 1993; Paczyński 1998; Woosley & Bloom 2006; Cano et al. 2017b) or when two compact objects like a neutron star (NS) and a black hole (BHs, Narayan et al. 1992) or two NSs (Duncan & Thompson 1992; Usov 1992; Thompson 1994; Metzger et al. 2011) merge, as exhibited by the quasi-simultaneous gravitational-wave (GW) and electromagnetic detections in GW170817/GRB170817A (Abbott et al. 2017a). According to the duration of the main episode (T_{90}),¹ usually described by an empirical “Band” function (Band et al. 1993), GRBs are further divided into two categories: short GRBs (sGRBs) with $T_{90} \leq 2$ s and long GRBs (lGRBs) with $T_{90} \geq 2$ s (Mazets et al. 1981; Kouveliotou et al. 1993). SGRBs are the outcome of the merger of compact objects, whereas lGRBs are the product of the collapse of massive stars. Irrespective of the progenitor, a relativistic collimated jet is launched producing the prompt GRB emission via internal shocks or magnetic reconnections, and subsequently afterglow radiation when it interacts with the external environment. However, during the core-collapses of dying massive stars or the coalescence of compact objects, a cocoon / shock breakout emission could also be expected (e.g., see Nagakura et al. 2014; Murguia-Berthier et al. 2014; Lazzati et al. 2017, 2018; Nakar & Piran 2017; Gottlieb et al. 2018a).

As the GRB jet makes its way through the stellar envelope of an enveloped star or as it traverses inside the neutrino/magnetically-driven wind previously ejected during the binary NS merger, the energy deposited laterally is significant and, therefore, will form a cocoon that engulfs the jet (Ramirez-Ruiz et al. 2002; Pe’er et al. 2006; Murguia-Berthier et al. 2014; Nagakura et al. 2014). The luminosity of the jet during the propagation phase should be similar to that seen during the prompt GRB phase. This indicates that the cocoon may be provided with an amount

* E-mail: nifraija@astro.unam.mx

¹ From 5% to 95% of the total counts observed from a burst’s prompt emission occur within a time interval denoted by T_{90} .

of energy that is similar to that of a prompt emission. Nagakura et al. (2014) numerically showed that when a low-luminosity jet is considered, a hot cocoon confining the jet is formed. Murguia-Berthier et al. (2014) found that when the jet has low or high luminosity a weak cocoon emission is expected from a typical sGRB. As soon as the relativistic jet reaches the outermost material, the cocoon emerges with a wider angle than the GRB jet and expands along the jet's axis. Beyond the outermost material, the external pressure decreases abruptly, so the cocoon can accelerate and expand until it becomes transparent. Accelerated material from the cocoon fireball will continue moving in the jet's axis. The cocoon fireball with a typical ejected mass in the range of $\sim 10^{-6} - 10^{-4} M_{\odot}$ can be modelled as a quasi-spherical outflow with Lorentz factor $\Gamma \sim 2 - 3$ (Murguia-Berthier et al. 2014; Nagakura et al. 2014; Rezzolla & Kumar 2015) once it emerges from the breakout, although in some scenarios the Lorentz factor could achieve values of ~ 10 (Nakar & Piran 2017). The quasi-spherical material interacting with the external medium could contribute to the electromagnetic emission in several frequencies and temporal scales, so afterglow measurements may help us learn about the progenitor and constrain the density of the external environment (Fraija et al. 2016a,b).

The first detectable electromagnetic signature from a star explosion might occur when a shock breaks out and travels outward through the stellar envelope. Before it breaks forth, radiation dominates the shock, and after, when the optical depth becomes unity, the photons in the trough layer all leave at once, producing an intense and brief electromagnetic signature that goes from UV to gamma rays. Photons in the UV band are expected in the Newtonian regime (Colgate 1974; Falk 1978; Klein & Chevalier 1978; Imshennik et al. 1981; Wang et al. 2000; Enzman & Burrows 1992; Katz et al. 2012), and up to gamma-rays are expected in the relativistic regime (Katz et al. 2010; Nakar & Sari 2010, 2012). Once this shock-breakout material makes contact with the circumstellar medium, it will be powerless to affect the launching phase of the expansion until the quantity of material that is swept up is equal to the mass that was ejected. At this point, the ejecta masses had already started to gradually slow down and take on a velocity structure, with the material moving more quickly at the front of the ejected mass than at the back.

In several circumstances, the density profile of the circumburst medium around GRBs in the form $\propto r^{-k}$ with $k = 0$ (ISM) and $k = 2$ (stellar wind) has been used to describe the multiwavelength afterglow observations (e.g., see Yi et al. 2013; Liang et al. 2013; Kumar et al. 2008; Kouveliotou et al. 2013; Li et al. 2020; Fraija et al. 2017a, 2019b). For instance, Yi et al. (2013) looked at over a dozen GRBs and came to the conclusion that the circumburst environment was not homogenous nor a stellar-wind medium, but rather a mixture of the two, whose density-profile index falls between 0.4 and 1.4. After analyzing a bigger sample of 146 GRBs, Liang et al. (2013) reported a preferred index around $k \sim 1$. Furthermore, Kumar et al. (2008) found a density-profile index of $k = 2.5$ after investigating the possibility that accretion of a stellar envelope in a BH could explain the plateau phase found in some X-ray light curves. On the other hand, Moriya & Tominaga (2012) demonstrated that the spectrum variety of Type II bright supernovae (SN IIa) may be partially explained by variations in the density slope of the dense wind caused by non-steady mass loss. They advocated for a $\propto r^{-k}$ wind density structure and found that variations in spectral SN development are substantially dependent on the k index. Kouveliotou et al. (2013) performed a multi-wavelength analysis and modeled the GRB 130427A observations from radio to GeV energy bands with the standard synchrotron model. They reported that the multiwavelength afterglow observations were consistent with a density profile index between $k = 0$ and $k = 2$. SN 2020bvc is a recent case study into the possible relationship between SN and GRB emission and a stratified environment (Izzo et al. 2020). The X-ray light curve is in good agreement with expectations for a decelerated material in a stratified medium with $k = 1.5$, which is consistent with the GRB-associated, broad-lined Ic SN 1998bw. Several bursts of multiwavelength data have shown an afterglow transition from stellar wind environment to ISM (e.g., see Dai & Wu 2003; Kamble et al. 2007; Jin et al. 2009; Li et al. 2020; Fraija et al. 2017a, 2019b).

A large half-opening angle, the essential parameter for characterizing the cone-shaped area from which the relativistic outflow of a GRB originates, and the low luminosity in the gamma-ray band are two factors that have led some authors to classify GRBs as low-luminosity (ll)GRBs (Bromberg et al. 2011; Hjorth 2013; Schulze et al. 2014; Cano et al. 2017a). Similarly, llGRBs are associated with the shock breakout and cocoon materials (Bromberg et al. 2011; Murguia-Berthier et al. 2014; Barniol Duran et al. 2015). Because we consider the synchrotron emission of an outflow with a large opening angle (quasi-spherical), we apply this scenario to bursts with low luminosity. So far, there are five confirmed llGRB: GRB 980425 (Galama et al. 1998), GRB 031203 (Thomsen et al. 2004), GRB 060218 (Campana & et al. 2006), GRB 100316D (Cano et al. 2011) and GRB 171205A (Izzo et al. 2019). Synchrotron afterglow scenarios from a quasi-spherical material used to describe some llGRBs assumed either a constant density medium ($k = 0$) or a stellar wind ($k = 2$) as the circumburst medium, without considering the self-absorption regime, or that the fraction of electrons accelerated in the shock front could be less than unity. For instance, Barniol Duran et al. (2015) considered a wind shock-breakout model to fit the radio and X-ray data of GRB 980425 introducing two power-law electron distributions; one distribution for the radio wavelengths and another for X-ray data. In addition, they explained the prompt emission of GRB 060218 as arising from a mildly relativistic shock breakout (with a low value of Lorentz factor ~ 1.3), and its radio afterglow from the interaction between ejecta and the surrounding wind medium. The authors suggested that the X-ray and radio emission might originate from different electron populations or emission processes. To overcome this limitation, we have systematically generalized the afterglow model to a stratified medium with a general index $0 < k < 3$, allowing for the analysis of environments beyond ISM or wind, such as those predicted for merger ejecta or progenitors with non-steady mass loss (Ramirez-Ruiz et al. 2005; Moriya & Tominaga 2012). Furthermore, we extend the synchrotron spectra to include both the coasting phase as well as the fraction of electrons accelerated by the shock front and self-absorption regime, crucial for modeling early radio emission (Urata et al. 2019) and to unify the relativistic and sub-relativistic regimes, enabling continuous modeling from prompt cocoon or breakout material to late-time emission.

In this paper, we extend the analytical synchrotron afterglow scenario of the quasi-spherical outflow model that was previously utilized to characterize the earlier X-ray and radio afterglow data in GRB 170817A (see [Frajia et al. 2019c](#)). Firstly, we assume that the external medium surrounding the burst is stratified, with a profile density of $\propto r^{-k}$ with a corresponding value of k between $0 \leq k < 3$. Secondly, we extend the synchrotron scenario to the self-absorption regime. Thirdly, we derive the coasting phase when the quasi-spherical outflow is not yet decelerated, and finally, we consider that only a fraction of electrons are accelerated by the shock front. We use this model to interpret a sample of IIGRBs, bursts with late observations. We consider the database of the Burst Area Telescope (BAT) instrument on board the Neil Gehrels *Swift* with sGRBs located between 100 and 200 Mpc. This paper is arranged as follows: In Section §2 we derive the synchrotron scenario of the quasi-spherical outflow decelerated in a stratified circumburst medium. In Section §3, we apply the proposed analytical model to describe the multi-wavelength observations of a sample of bursts and provide constraints to other ones. In Section §4, we synthesize prior research and clarify distinctions with the current scenario. Finally, in Section §5, we provide a summary of our work and some concluding remarks.

2 QUASI-SPHERICAL OUTFLOW IN A STRATIFIED MEDIUM

During the initial coasting phase, the relativistic outflow is not impacted by the circumburst medium. Hence, in the coasting phase, the bulk Lorentz factor remains constant $\Gamma = \Gamma_0$ and the radius develops as $r = \frac{c\beta_0 t}{(1+z)}$ with $\beta_0 = \sqrt{\Gamma_0^2 - 1}/\Gamma_0$. After the coasting phase, the deceleration phase begins. Here the ejected mass gains a velocity structure, with the matter in the front of the expelled mass moving faster than the one in the rear ([Sari & Mészáros 2000](#)). The quasi-spherical material then transmits a considerable portion of its energy to its surrounding environment, leading to a forward shock. [Tan et al. \(2001\)](#) investigated the ejected mass's acceleration at relativistic and sub-relativistic velocities. They discovered that at the sub- and ultra-relativistic limit, the isotropic-equivalent kinetic energy may be represented as a power-law velocity distribution provided by

$$E(\beta\Gamma) = \tilde{E} \left[(\Gamma\beta)^{-(5.35 - \frac{2}{\gamma_p})\frac{1}{q}} + (\Gamma\beta)^{-(1.58 - \frac{1}{\gamma_p})\frac{1}{q}} \right]^{q\gamma_p}, \quad (1)$$

where $\gamma_p = 1 + 1/n_p$ with $n_p = 3$ the polytropic index, \tilde{E} is the fiducial energy, $\beta = \sqrt{\Gamma^2 - 1}/\Gamma$ and $q = 4.1$ is a parameter (e.g., see [Tan et al. 2001](#)). In the limiting cases, Eq. 1 becomes $E \simeq \tilde{E} (\Gamma\beta)^{-(1.58\gamma_p - 1)}$ at the relativistic velocities ($\beta\Gamma \gg 1$), and $E \simeq \tilde{E} (\Gamma\beta)^{-(5.35\gamma_p - 2)}$ at the sub-relativistic velocities ($\Gamma\beta \ll 1$). Additionally, we consider that a quasi-spherical material is decelerated in a stratified density profile given by $n(r) = n_k \left(\frac{r}{r_0}\right)^{-k}$ with $0 \leq k < 3$. For instance, with a density profile index of $k = 2$, $n_k r_0^k = A_{st} 3 \times 10^{35} \text{ cm}^{-1}$, with A_{st} the parameter of density profile. Hereafter, we refer to quantities in the observer and comoving frames with unprimed and primed terms, respectively. We also adopt the convention $Q_x = Q/10^x$ in c.g.s. units.

2.1 Mildly- relativistic regime

At the relativistic velocities $E \simeq \tilde{E} (\Gamma\beta)^{-\alpha_s}$ with $1.1 \leq \alpha_s \leq 2.1$, the adiabatic evolution of the forward shock with an isotropic equivalent-kinetic energy becomes $\tilde{E} (\beta\Gamma)^{-\alpha_s} = \frac{4\pi}{3} m_p c^2 n(r) r^3 \beta^2 \Gamma^2$ (Blandford-McKee solution; [Blandford & McKee 1976](#)). Given a radial distance $r = \frac{2c\beta\Gamma^2 t}{(1+z)}$, the bulk Lorentz factor evolves as

$$\Gamma \propto (1+z)^{-\frac{k-3}{\alpha_s+8-2k}} A_{st}^{-\frac{1}{\alpha_s+8-2k}} \beta^{-\frac{\alpha_s+5-k}{\alpha_s+8-2k}} \tilde{E}^{\frac{1}{\alpha_s+8-2k}} t^{\frac{k-3}{\alpha_s+8-2k}}, \quad (2)$$

where the deceleration time evolves as $t_{\text{dec}} \propto (1+z)^{\frac{1}{k-3}} A_{st}^{\frac{1}{k-3}} \beta^{\frac{\alpha_s+5-k}{k-3}} \tilde{E}^{-\frac{1}{k-3}} \Gamma^{\frac{\alpha_s+8-2k}{k-3}}$. When the quasi-spherical material enters the post-jet-break decay phase ($\Gamma \simeq 1/\theta_c$, with θ_c the opening angle), the bulk Lorentz factor evolves as

$$\Gamma \propto (1+z)^{-\frac{k-3}{\alpha_s+6-2k}} A_{st}^{-\frac{1}{\alpha_s+6-2k}} \beta^{-\frac{\alpha_s+5-k}{\alpha_s+6-2k}} \tilde{E}^{\frac{1}{\alpha_s+6-2k}} t^{\frac{k-3}{\alpha_s+6-2k}}, \quad (3)$$

where the break time becomes $t_{\text{br}} \propto (1+z)^{\frac{1}{k-3}} A_{st}^{\frac{1}{k-3}} \beta^{\frac{\alpha_s+5-k}{k-3}} \tilde{E}^{-\frac{1}{k-3}} \theta_c^{-\frac{\alpha_s+8-2k}{k-3}}$. Given the non evolution of bulk Lorentz factor ($\Gamma \propto t^0$) during the coasting phase, the evolution of the bulk Lorentz factor can be summarized as

$$\Gamma \propto \begin{cases} t^0, & t < t_{\text{dec}}, \\ t^{\frac{k-3}{\alpha_s+8-2k}}, & t_{\text{dec}} \leq t \leq t_{\text{br}}, \\ t^{\frac{k-3}{\alpha_s+6-2k}} & t_{\text{br}} \leq t. \end{cases} \quad (4)$$

For the case of $\alpha_s = 0$ and $k = 0$, the isotropic equivalent-kinetic energy is constant, and the evolution of the bulk Lorentz factor $\Gamma \propto t^0$, $\propto t^{-\frac{3}{8}}$, and $\propto t^{-\frac{1}{2}}$ are obtained ([Sari & Piran 1999; Sari et al. 1998, 1999](#)).

In forward-shock models, the arrangement of the accelerated electrons depends on their Lorentz factors (γ_e), and the electron power index p . They follow the distribution $N(\gamma_e) d\gamma_e \propto \gamma_e^{-p} d\gamma_e$ for $\gamma_m \leq \gamma_e$, where $\gamma_m = \frac{m_p}{m_e} g(p) \varepsilon_e (\Gamma - 1) \zeta_e^{-1}$ is the minimum electron Lorentz factor, m_p and m_e the proton and electron mass, respectively, ε_e the fraction of energy given to accelerate electrons, ζ_e the fraction of electrons that were accelerated by the shock front ([Fan & Piran 2006](#)) and $g(p) = \frac{p-2}{p-1}$. The energy density $U = [(\hat{\gamma}\Gamma + 1)/(\hat{\gamma} - 1)](\Gamma - 1)n(r)m_p c^2$ with $\hat{\gamma}$ the adiabatic index ([Huang et al. 1999](#)) and its respective fraction given to magnetic field (ε_B) are used to calculate the intensity of the blastwave's

comoving magnetic field $B'^2/(8\pi) = \varepsilon_B U$. The cooling electron Lorentz factor is $\gamma_c = \frac{6\pi m_e c}{\sigma_T} (1+Y)^{-1} \Gamma^{-1} B'^{-2} t^{-1}$, where σ_T is the cross-section in the Thomson regime, c is the speed of light and Y is the Compton parameter (Sari & Esin 2001; Wang et al. 2010). The synchrotron spectral breaks and the synchrotron radiation power per electron in the comoving frame are given by $\nu_i = \frac{q_e}{2\pi m_e c} (1+z)^{-1} \Gamma \gamma_i^2 B'$ (with $i = m$ and c) and $P_{\nu_m} \simeq \frac{\sqrt{3} q_e^3}{m_e c^2} (1+z)^{-1} \Gamma B'$, respectively, with q_e the elementary charge (e.g., see Sari et al. 1998; Fraija 2015). The synchrotron spectral breaks in the self-absorption regime are derived from $\nu_{a,1} = \nu_c \tau_{0,m}^{\frac{3}{5}}$, $\nu_{a,2} = \nu_m \tau_{0,m}^{\frac{2}{p+4}}$ and $\nu_{a,3} = \nu_m \tau_{0,c}^{\frac{3}{5}}$ with the optical depth given by $\tau_{0,i} \simeq \frac{5}{3-k} \frac{q_e n(r) r}{B' \gamma_i^5}$ (Panaitescu & Mészáros 1998). Considering the total number of emitting electrons $N_e = n(r) \frac{4\pi}{3-k} r^3$, the radiation power and the synchrotron spectral breaks, the maximum flux becomes $F_{\nu, \text{max}} = \frac{(1+z)^2}{4\pi d_z^2} N_e P_{\nu_m}$, where $d_z = (1+z) \frac{c}{H_0} \int_0^z \frac{d\tilde{z}}{\sqrt{\Omega_M(1+\tilde{z})^3 + \Omega_\Lambda}}$ (Weinberg 1972) is the luminosity distance. We assume for the cosmological constants a spatially flat universe Λ CDM model with $H_0 = 69.6 \text{ km s}^{-1} \text{ Mpc}^{-1}$, $\Omega_M = 0.286$ and $\Omega_\Lambda = 0.714$ (Planck Collaboration et al. 2016).

2.2 Sub-relativistic regime

During this regime, the isotropic equivalent-kinetic energy becomes $E \simeq \tilde{E} \beta^{-\alpha_s}$ with $3 \leq \alpha_s \leq 5.2$, and the dynamics of the non-relativistic ejecta mass is described by the Sedov-Taylor solution. Then, given the evolution of the radius $r \propto (1+z)^{-\frac{\alpha_s+2}{\alpha_s+5-k}} A_{\text{st}}^{-\frac{1}{\alpha_s+5-k}} \tilde{E}^{\frac{1}{\alpha_s+5-k}} t^{\frac{\alpha_s+2}{\alpha_s+5-k}}$, the velocity can be written as

$$\beta \propto (1+z)^{\frac{3-k}{\alpha_s+5-k}} A_{\text{st}}^{-\frac{1}{\alpha_s+5-k}} \tilde{E}^{\frac{1}{\alpha_s+5-k}} t^{\frac{k-3}{\alpha_s+5-k}}, \quad (5)$$

where the deceleration time evolves as $t_{\text{dec}} \propto \beta^{\frac{\alpha_s+5-k}{k-3}}$. During the coasting phase, the velocity of the quasi-spherical material is not altered and therefore becomes constant ($\beta \propto t^0$). Taking into account the coasting and deceleration phase, the evolution of the velocity can be summarized as

$$\beta \propto \begin{cases} t^0, & t < t_{\text{dec}}, \\ t^{\frac{k-3}{\alpha_s+5-k}}, & t_{\text{dec}} \leq t. \end{cases} \quad (6)$$

For the case of $\alpha_s = 0$ and $k = 0$, the evolution of the velocity in Sironi et al. (2013) is recovered.

For the sub-relativistic regime, we assume that the shocked-accelerated electrons have the same distribution as the previous relativistic regime $\frac{dn}{d\gamma_e} \propto \gamma_e^{-p}$ for $\gamma_e \geq \gamma_m$, with $\gamma_m \propto \beta^2$ the Lorentz factor of the lowest-energy electrons. In this case, the magnetic field evolves as $B' \propto A_{\text{st}}^{\frac{1}{2}} \beta^{\frac{2-k}{2}} t^{-\frac{k}{2}}$ and the Lorentz factor of the highest energy electrons, which are efficiently cooled by this process as $\gamma_c \propto A_{\text{st}}^{-1} \beta^{k-2} t^{k-1}$. The synchrotron spectral (characteristic and cooling) breaks and the synchrotron radiation power per electron evolve as $\nu_m \propto A_{\text{st}}^{\frac{1}{2}} \beta^{\frac{10-k}{2}} t^{-\frac{k}{2}}$, $\nu_c \propto A_{\text{st}}^{-\frac{3}{2}} \beta^{\frac{3k-6}{2}} t^{\frac{3k-4}{2}}$ and $P_{\nu, \text{max}} \propto A_{\text{st}}^{\frac{1}{2}} \beta^{\frac{2-k}{2}} t^{-\frac{k}{2}}$, respectively. Considering the total number of emitting electrons $N_e \propto A_{\text{st}} \beta^{3-k} t^{3-k}$, the radiation power, and the synchrotron spectral breaks, the maximum flux varies as $F_{\nu, \text{max}} \propto A_{\text{st}}^{\frac{3}{2}} \beta^{\frac{8-3k}{2}} t^{\frac{3(2-k)}{2}}$. In the self-absorption regime, the synchrotron spectral breaks evolve as $\nu_{a,1} \propto A_{\text{st}}^{\frac{4}{5}} \beta^{-\frac{4k+5}{5}} t^{\frac{3-4k}{5}}$, $\nu_{a,2} \propto A_{\text{st}}^{\frac{p+6}{2(p+4)}} \beta^{\frac{10p-kp-6k}{2(p+4)}} t^{\frac{4-kp-6k}{2(p+4)}}$, and $\nu_{a,3} \propto A_{\text{st}}^{\frac{9}{5}} \beta^{\frac{15-9k}{5}} t^{\frac{8-9k}{5}}$ for $\nu_{a,1} \leq \nu_m \leq \nu_c$, $\nu_m \leq \nu_{a,2} \leq \nu_c$ and $\nu_{a,3} \leq \nu_c \leq \nu_m$, respectively (details of the derivation are explicitly written in Fraija et al. 2021a).

2.3 Analysis and Description

Appendix A summarizes our analytical synchrotron forward-shock model from the deceleration of a quasi-spherical material in a stratified environment during the relativistic and sub-relativistic regimes. In addition, we include the evolution of the quasi-spherical material in the coasting and post-jet break decay stages. Table 1 and Table 2 summarize, for each cooling condition, the evolution of the synchrotron fluxes and the closure relations respectively.

Table 3 shows the evolution of the density parameter in each cooling condition of the synchrotron afterglow model from a quasi-spherical material in both the relativistic and sub-relativistic regimes. For each regime, the coasting, deceleration and post-jet break decay phases are exhibited. For instance, in the sub-relativistic regime the synchrotron flux as a function of the density parameter is given by $F_{\nu} : \propto A_{\text{st}}^{\frac{4\alpha_s+13}{3(\alpha_s+5-k)}}$ for $\nu_{a,1} < \nu < \nu_m$, $\propto A_{\text{st}}^{\frac{19+p(\alpha_s-5\alpha_s)+5}{4(\alpha_s+5-k)}}$ for $\nu_m < \nu < \nu_c$ and $A_{\text{st}}^{\frac{p(\alpha_s-5)+2(\alpha_s+5)}{4(\alpha_s+5-k)}}$ for $\nu_c < \nu$, and in the relativistic regime as $F_{\nu} : \propto A_{\text{st}}^{\frac{4(\alpha_s+3)}{3(\alpha_s+8-2k)}}$ for $\nu_{a,1} < \nu < \nu_m$, $\propto A_{\text{st}}^{\frac{16+\alpha_s(p+5)}{4(\alpha_s+8-2k)}}$ for $\nu_m < \nu < \nu_c$ and $A_{\text{st}}^{\frac{\alpha_s(p+2)}{4(\alpha_s+8-2k)}}$ for $\nu_c < \nu$. On the other hand, the synchrotron light curve after the jet break as a function of the density parameter is given by $F_{\nu} : \propto A_{\text{st}}^{\frac{4(\alpha_s+1)}{6+5\alpha_s+p(\alpha_s-2)}}$ for $\nu < \nu_m$, $\propto A_{\text{st}}^{\frac{(p+2)(\alpha_s-2)}{4(\alpha_s+6-2k)}}$ for $\nu_m < \nu < \nu_c$ and $A_{\text{st}}^{\frac{(p+2)(\alpha_s-2)}{4(\alpha_s+6-2k)}}$ for $\nu_c < \nu$. These relations show that any variation of the density parameter, in both the relativistic and lateral expansion phases, will be more pronounced in the first two cases, that is in $\nu < \nu_m$ and $\nu_m < \nu < \nu_c$. This points out that this variation will be enhanced in low-energy bands, namely radio and optical. It is also important to note that this feature will be intensified as the value of the velocity distribution parameter α_s is increased, as well as that of the stratification parameter k . Given this discussion, a transition between different circumburst density parameters will be more efficiently observed in the radio and optical bands with high values of stratification and of the velocity distribution parameter. On the other hand, this feature will also vary between both phases. In the relativistic phase, the second regime ($\nu_m < \nu < \nu_c$) will enhance the variation of the density, while in the lateral expansion phase, it is the first regime ($\nu < \nu_m$) that amplifies this difference. Therefore, it is expected that the contrast will be more easily observed in the optical band during the relativistic phase, while in the lateral expansion phase, this will be simpler in lower energy bands, such as radio.

The synchrotron spectral breaks during the deceleration phase evolve as $\nu_m \propto t^{-\frac{30+k(\alpha_s-8)}{2(\alpha_s+5-k)}}$ and $\nu_c \propto t^{\frac{k(4+3\alpha_s)-4\alpha-2}{2(\alpha_s+5-k)}}$ for the non-relativistic regime, and as $\nu_m \propto t^{-\frac{24+k(\alpha_s-6)}{2(\alpha_s+8-2k)}}$ and $\nu_c \propto t^{-\frac{(\alpha_s+2)(4-3k)}{2(\alpha_s+8-2k)}}$ for the relativistic regime. In a similar way to the work by [Giblin et al. \(1999\)](#) for the relativistic regime using the standard synchrotron afterglow model, we propose the evolution of the estimated flux a useful tool for locating the synchrotron emission from the non-relativistic and relativistic quasi-spherical material. [Giblin et al. \(1999\)](#) studied the evolution of spectral indexes and break energy of the prompt episode ($T_{90} \approx 40$ s) followed by a smooth emission tail that lasted ~ 400 s observed in GRB 980923. They found that the low-energy spectral index in the smooth tail evolved as the synchrotron cooling break $\propto t^{-0.52 \pm 0.12}$, thus concluding that the forward-shock had started during the prompt episode. Afterwards, spectral analyses of burst tails were performed to identify early afterglow emissions (e.g., see [Barthelmy et al. 2005](#); [Yamazaki et al. 2006](#)).

3 APPLICATION

3.1 A sample of LLGRBs: GRB 980425, 031203, 060218, 100316D, 130603B, 150101B and 171205A

3.1.1 GRB 980425

GRB 980425 was detected on April 25, 1998 by the BATSE instrument on board the *Compton Gamma Ray Observatory* (CGRO) and both by the Gamma-ray Burst Monitor (GRBM) and the second Wide Field Cameras (WFC) on board the *BeppoSAX*, respectively. ([Kippen & the BATSE GRB team 1998](#); [Soffitta et al. 1998](#)). The duration of the burst is about 30 s. Three days after the trigger, the *Australian Telescope Compact Array* (ATCA) found three radio sources within the 8 arcmin error box. The brightest source was located at coordinates RA(J2000)=19h 35m 03.31s and Dec(J2000)= $-52^{\circ}50'44.7''$, which coincided with the position of SN 1998bw ([Wieringa et al. 1998](#)). This association with the SN host galaxy ESO 184-G82 and spectroscopy led to the determination of the burst redshift $z = 0.0085 \pm 0.0002$ ([Tinney et al. 1998](#)). The isotropic-equivalent energy in the $1 - 10^4$ keV energy range was $E_{\gamma, \text{iso}} = (9.29 \pm 0.35) \times 10^{47}$ erg. The corresponding total fluence in the gamma-ray (30 - 400 keV) and X-ray (2 - 30 keV) bands were 3.40×10^{-6} erg cm $^{-2}$ and 1.99×10^{-6} erg cm $^{-2}$, respectively. The radio observations at 20, 13, 6 and 3 cm began to be collected with ATCA 3 days after the trigger time. These radio observations were performed during almost 81 days.

3.1.2 GRB 031203

On December 03 2003 at 22:01:28 UTC, GRB 031203 was detected by the *INTEGRAL*/IBIS instrument at coordinates RA(J2000)= $08^{\text{h}}02^{\text{m}}30^{\text{s}}$ and Dec(J2000)= $-39^{\circ}50'49''$ ([Gotz et al. 2003](#)) with a duration T_{90} in the 15 – 200 keV band of ~ 20 s. Subsequent follow-up observations were carried out by the *SMARTS* telescope ([Bailyn et al. 2003](#); [Santos-Lleo et al. 2003](#)), the Newton X-ray Multiple Mirror *XMM-Newton* ([Frail 2003](#)), the Advanced CCD Imaging Spectrometer (ACIS) instrument onboard the Chandra X-ray Observatory (CXO) and the Very Large Array (VLA), which allowed the discovery of radio and X-ray afterglows. The XMM Observatory reported an X-ray flux in the 2- 10 keV energy range of $(3.95 \pm 0.09) \times 10^{-13}$ erg cm $^{-2}$ s $^{-1}$. The CXO reported an X-ray count rate in the 2- 10 keV energy range of 5.6×10^{-4} s $^{-1}$. The redshift of GRB 031203 was determined to be $z = 1.055 \pm 0.0001$ ([Prochaska et al. 2004](#); [Watson et al. 2004](#); [Margutti et al. 2007](#)). Spectral analysis revealed an isotropic-equivalent energy in the $1 - 10^4$ keV energy range of $E_{\gamma, \text{iso}} = 1.67_{-0.10}^{+0.04} \times 10^{50}$ erg. At ≈ 10 hours, the corresponding isotropic X-ray luminosity was 9×10^{42} erg, almost 10^3 fainter than the usual observed burst. At 8.5 GHz, the peak luminosity corresponded to $\approx 10^{29}$ erg s $^{-1}$ Hz $^{-1}$, 10^2 fainter than the usual observed burst.

3.1.3 GRB 060218

GRB 060218 was detected by the *Swift* / BAT instrument on February 18, 2006, at 03:34:30 UT in the coordinates RA(J2000)= $03^{\text{h}}21^{\text{m}}37^{\text{s}}$ and Dec(J2000)= $+16^{\circ}51'58''$ ([Cusumano et al. 2006](#)). Afterglow confirmation from the X-ray Telescope (XRT) instrument aboard *Swift* was a $T + 153$ s detecting a bright, fading point source ([Kennea et al. 2006](#)). Simultaneously, the Ultraviolet and Optical Telescope (UVOT) aboard *Swift* tracked this event for up to 1036 s after the initial trigger ([Marshall et al. 2006](#)). The redshift of the event was determined by its association with a host galaxy at $z = 0.0331$ ([Mirabal & Halpern 2006](#)). This event was associated with SN 2006aj. The XRT instrument monitored GRB 060218 in the windowed-timing (WT) mode with a spectrum exposure of 2.6 ks and the Photon Counting (PC) mode with a spectrum exposure of 52.8 ks. The best-fit values for the intrinsic absorption column densities were $3.58_{-0.07}^{+0.07} \times 10^{21}$ cm $^{-2}$ and $4.4_{-0.6}^{+0.6} \times 10^{21}$ cm $^{-2}$ for the WT and PC modes, respectively. A black-body component exhibiting a decreasing temperature of 0.17 keV and a simultaneous increase in brightness with time was observed. This black-body was observed at 7×10^3 s with a temperature of 0.10 ± 0.05 keV. At 1.2×10^5 s, the black-body was detected by UVOT with a temperature of $3.7_{-0.9}^{+1.9}$ eV, implying an expansion with a sub-relativistic velocity.

3.1.4 GRB 100316D

GRB 100316D was detected by the *Swift* / BAT instrument on 16 March 2010 12:44:50 UT at RA(J2000)= $07^{\text{h}}10^{\text{m}}28^{\text{s}}$ and Dec(J2000)= $-56^{\circ}16'40''$ ([Stamatikos et al. 2010](#)). Posterior analysis of the BAT light curve photometry found temporal and spectral similarities with SN GRB 060218/2006aj ([Sakamoto et al. 2010](#)). The identification of the redshift was done using observations carried out by the VLT Collaboration ([Vergani et al. 2010](#)). Using data from the X-shooter spectrograph, ([Chornock et al. 2010](#)) reported the association of GRB 100316D with a galaxy located at $z = 0.059$. This event was associated with SN 2010bh. The XRT instrument monitored this burst in the WT mode with a spectrum exposure of 594 s and the PC mode with a spectrum exposure of 3.8 ks. The best-fit values for the intrinsic absorption column densities were $1.06_{-0.06}^{+0.06} \times 10^{22}$ cm $^{-2}$ and $5.6_{-5.5}^{+17.9} \times 10^{21}$ cm $^{-2}$ for the WT and PC modes, respectively. This burst was also detected by Gemini-South and HST for almost two weeks. A black body component contributing only $\sim 3\%$ of the X-ray flux in the 0.3 - 10 energy range was detected with a temperature of 0.14 ± 0.01 keV and a luminosity of $3 - 4 \times 10^{46}$ erg s $^{-1}$.

3.1.5 GRB 130603B

On 3 June 2013 at 15:49:14, GRB 130603B was simultaneously detected by the BAT instrument aboard the *Swift* satellite ([Melandri et al. 2013](#)) and by Konus-Wind ([Tanvir et al. 2013](#)). Its location was found to be at R.A. = $+21^{\text{h}}23^{\text{m}}27^{\text{s}}$, Dec = $-53^{\circ}02'02''$ (J2000). According to the BAT instrument, it had a duration of $T_{90} \approx 0.18 \pm 0.02$ s in the 15-350 keV band ([Barthelmy et al. 2013](#)), which places it in the sGRB class. The *Swift*/XRT instrument began to

observe the error box at $T + 43$ s discovering an uncatalogued X-ray source at the location of the burst (Evans et al. 2013; Kennea et al. 2013). Subsequent X-ray observations were performed days later by the *XMM-Newton* telescope (Fong et al. 2013b). Using ground telescopes, this burst was followed-up by the twin *Magellan* telescopes in the optical band (Foley et al. 2013), whereas in radio by the VLA (Very Large Array) (Fong et al. 2013a). Optical observations allowed the determination of the redshift of $z = 0.3568 \pm 0.0005$ (Cucchiara et al. 2013). Optical and near-IR observations of the event also demonstrated the presence of excess near-IR emission matching a KN (Berger et al. 2013).

3.1.6 GRB 150101B

The *Swift*/BAT and the *Fermi*/GBM instruments triggered GRB 150101B on January 1, 2015, at 15:23 and at 15:24:34.468, respectively (Cummings et al. 2015; Burns et al. 2018) with an estimated duration of about $T_{90} = 0.08 \pm 0.93$ s. Features of absorption in the spectrum at lower frequencies were carried out with *Magellan*/Baade, *VLT* and *TNG* (Fong et al. 2016), associated with a young host galaxy located in the constellation Virgo at $z = 0.1343 \pm 0.0030$. The total fluence and isotropic-equivalent gamma-ray energy in the energy range of 10 - 1000 keV were $\sim 10^{-7}$ erg cm $^{-2}$ and $E_{\gamma,\text{iso}} \sim 4.7 \times 10^{48}$ erg, respectively (Troja et al. 2018), which corresponded to one of the lowest energies reported by Swift/BAT. The characteristics of this burst were very similar to those of the gravitational wave event GW170817, associated with a merger of a binary NS stars (Burns et al. 2018; Troja et al. 2018).

3.1.7 GRB 171205A

The BAT instrument triggered and localized GRB 171205A on 2017 December 5 at 07:20:43.9 UT (D'Elia et al. 2017). With an isotropic luminosity $L_{\text{iso},\gamma} = 3.0 \times 10^{47}$ erg s $^{-1}$ and a duration of $T_{90} = 190.0 \pm 35.0$ s in the 15-150-keV energy range (Barthelmy et al. 2017), GRB 171205A was classified as a long llGRB (Izzo et al. 2019). This GRB was also detected by *Konus-Wind* (Frederiks et al. 2017) and was observed by *Swift*-XRT approximately 134 s after the BAT trigger (Kennea et al. 2017). *Swift*/UVOT confirmed a source consistent with the XRT position, so GRB 171205A was localized with coordinates RA(J2000)=11:09:39.547 and Dec(J2000)=−12:35:17.93 (Emery & D'Elia 2017). Several ground-based experiments were able to start observing the GRB in the optical and infrared bands only a few minutes after the initial BAT trigger, such as the CIBO collaboration (Melandri et al. 2017), the Gao-Mei-Gu station (Mao et al. 2017) and SNUCAM-II (Changsu Choi 2017), among others. Five days later, the 10.4-m Gran Telescopio Canarias (GTC) picked up on the emergence of the associated type Ic supernova (SN 2017iuk; de Ugarte Postigo et al. 2017) and SMARTS 1.3-m telescope (Cobb 2017). These detections were able to confirm the previous association between the burst and its host galaxy 2MASX J11093966-1235116 by Izzo et al. (2017a) and to also determine its redshift through the detection of absorption and emission lines at $z = 0.0368$ (Izzo et al. 2017b; D'Elia et al. 2018). GRB 171205A has been widely studied since it was the third nearest burst.

Since GRB 171205A was so close, Izzo et al. (2019) followed-up multi-wavelength observations using photometry and spectroscopy. They presented spectroscopic observations of the supernova SN 2017iuk taken across many time periods. Features at extraordinarily high expansion velocities ($\sim 1.15 \times 10^5$ km s $^{-1}$) were seen in the spectra during the first day following the burst. They used spectral synthesis models created for SN 2017iuk to demonstrate that the chemical abundances of these characteristics were distinct from those seen in the ejecta of SN 2017iuk at subsequent dates. The authors went on to demonstrate that a hot cocoon produced by the expansion and deceleration of an ultra-relativistic jet inside the progenitor star into the circumstellar medium was where the high-velocity characteristics are originating. During the first three days after the explosion, the cocoon material becomes transparent and dominates the electromagnetic emission and, later, the supernova emission begins to dominate the emission, and this cocoon quickly becomes opaque and is overtaken by the supernova emission.

3.2 Results and Discussion

Figures 1, 2, 3, 4, 5, 6 and 7 show the multiwavelength observations of GRB 980425, 031203, 060218, 100316D, 130603B, 150101B and 171205A, respectively, with the best-fit curves generated with our analytical scenario. We have considered the synchrotron radiation from the quasi-spherical material that decelerates in the stellar-wind environment (left panel) and ISM (right panel) for GRB 980425, 031203, 060218, 100316D and 171205A, and in the cases of the short bursts GRB 130603B and 150101B we consider the deceleration in ISM. We have implemented Markov-Chain Monte Carlo (MCMC) simulations using eight (E , A_{st} , Γ_0 , ε_B , ε_e , p , α_s , θ_c) parameters from the entire sample of llGRBs to determine the optimal values that characterize the multiwavelength observations with our synchrotron model. To describe the entire data in our sample, a total of 17,200 samples and 5,100 tuning steps were used. We only show Figure 8, which corresponds to GRB 980425, for displaying the best-fit parameter values with the respective median of the posterior distributions. In Table 4, the best-fit values are shown in red, and the median of the posterior distributions is presented.

The optimal values of the magnetic microphysical parameters fall within the range of $10^{-2} \lesssim \varepsilon_B \lesssim 10^{-1}$. The best-fit values of the microphysical parameter ε_e are within the range of $0.93 \times 10^{-2} \lesssim \varepsilon_e \lesssim 0.80$. Considering the magnetic equipartition parameter, the magnetization parameter is predicted to fall within a certain range. Taking into account the ε -values, the magnetization parameter is expected to be between 10^{-2} and 10^{-1} , which means that the material are moderately magnetic. There has been previous work with the intent to model afterglow observations of those GRBs we have considered in this work (Campana & et al. 2006; Daigne & Mochkovitch 2007; Fan et al. 2011; Margutti et al. 2013; Irwin & Chevalier 2016; Izzo et al. 2019; Maity & Chandra 2021). The values we have obtained for both microphysical parameters are in good agreement with the aforementioned studies. Santana et al. (2014) performed a statistical and bibliographical study to determine the distribution of ε_B in afterglow models. Their results showed that in both the optical and X-ray bands the distribution is rather wide, with optical measurements favoring $\varepsilon_B \sim 10^{-9} - 10^{-3}$ while X-ray observations prefer $\varepsilon_B \sim 10^{-5} - 10^{-1}$. The optimal values that we have obtained in our work are well in agreement with the later observations. In order to explain such large values of ε_B , Santana et al. (2014) addressed the possibility of bursts taking place in environments with particularly high seed magnetic fields (B_0).

The most suitable values of half-opening angles, lie in a range of $32^\circ \lesssim \theta_c \lesssim 55^\circ$, which are completely different from the values reported for half-jet opening angle of classical GRBs $\theta_j = 2^\circ - 10^\circ$ (Frail et al. 2001; Fong et al. 2015; Lamb et al. 2005; Mizuta & Ioka 2013; Jin et al. 2018). The large values found with our MCMC simulations agree with the multiwavelength observations which show no indication of late, steep decays over a time scale of weeks. It is worth noting that in some bursts show no indication of late steep decays in a time scale of days. For instance, GRB 190829A, located at $z = 0.0785 \pm 0.005$ (Valeev & et al. 2019) and classified as an intermediate-luminosity burst $E_{\gamma,\text{iso}} = (2.967 \pm 0.0032) \times 10^{50}$ erg, was one of the closest bursts, which was detected in TeV gamma- and X-rays by H.E.S.S. and *Swift*-XRT. The H.E.S.S. and *Swift*-XRT observations did not exhibit a jet break up to $\sim 10^6$ s, indicating that the half-jet opening angle was larger than $\gtrsim 17^\circ$ (e.g., see Fraija et al. 2021b; Lu-Lu et al. 2021; Sato et al. 2021).

The best-fit values of the power-law indexes for the electron distribution and the velocity distribution are in the ranges of $2.1 \lesssim p \lesssim 3.5$ and $2 \lesssim \alpha_s \lesssim 3$,

respectively, which is in the range of the ones reported in literature (Galama et al. 1998; Campana & et al. 2006; Daigne & Mochkovitch 2007; Fan et al. 2011; Margutti et al. 2013; Irwin & Chevalier 2016; Izzo et al. 2019; Maity & Chandra 2021). For instance, the late-time radio and X-ray observations and spectral/temporal analysis of GRB 100316D were modelled by Margutti et al. (2013), reporting a value close to $\alpha_s \sim 2.4$, and associating the progenitor as the emergence of the fastest rotating magnetar.

Efficiency is essential for understanding the gamma-ray emission mechanism. Considering the optimal values of the equivalent kinetic energies are $10^{50} \lesssim E \lesssim 10^{52}$ erg and the isotropic energies in gamma-rays during the early phase in the range of $10^{48} \lesssim E_{\gamma, \text{iso}} \lesssim 10^{50}$ erg, kinetic efficiencies fall around $\eta \approx 1 - 5\%$, which are typical compared to those values reported (Campana & et al. 2006; Daigne & Mochkovitch 2007; Fan et al. 2011; Margutti et al. 2013; Irwin & Chevalier 2016; Izzo et al. 2019; Maity & Chandra 2021).

The best-fit values of the density lie in the range of $0.1 \lesssim A_{\text{st}} \lesssim 10$. Barniol Duran et al. (2015) have considered the radio light curves of the late afterglow of GRB 980425, 031203, 060218 and 100316D. The initial bulk Lorentz factor values that are best-fitted fall within the $1.7 \lesssim \Gamma_0 \lesssim 4.9$, which is similar to the values found in other bursts. In the case of GRB 9804125, they used the non-relativistic phase description for an ISM medium, however the analytic behavior at late times increased with time, in contrast with observations. Therefore, they considered a wind medium with $A_{\text{st}} = 10$ and $p = 2.1$ which was able to reproduce the radio and X-ray observations. Their values were in agreement with Li & Chevalier (1999), who previously modeled the radio data of GRB 980425. They made the case for a surrounding wind medium. They presented two possible solutions, one with $A_{\text{st}} \approx 6$ for $\varepsilon_e \sim 1$ and $\varepsilon_B = 10^{-6}$, and another with $A_{\text{st}} \approx 0.04$ with $\varepsilon_e = \varepsilon_B = 0.1$. In the case of GRB 031203, Barniol Duran et al. (2015) and Soderberg et al. (2004) preferred an ISM model with $n \approx 0.1 \text{ cm}^{-3}$ due to the rather flat behavior of optical observations at late times. Regarding GRB 060218 and 100316D, Barniol Duran et al. (2015) found good agreement in the radio bands for a wind medium with $A_{\text{st}} = 1$ and $\varepsilon_B \sim 10^{-5}$, but their model predicted an X-ray flux lower than observations in both bursts. In the case of GRB 171205A, Maity & Chandra (2021) made the case for a stratified wind-like medium. They worked with both the standard isotropic afterglow model and a shock breakout model, for which they found that values of A_{st} in the range $\sim 0.1 - 1$ were able to reproduce radio measurements over 1000 days. Spectral and temporal analysis of the radio observations led to the conclusion that the ejecta was expanded to relativistic velocities (Galama et al. 1998). Waxman et al. (2007) and Margutti et al. (2013) modelled GRB 060218 and GRB 100316D the multiwavelength observations with a mildly relativistic material ($\Gamma = 1.5 - 2$), respectively.

Our model builds upon the work of Barniol Duran et al. (2015), who successfully explained the radio afterglows of GRBs 980425, 060218, and 100316D using a shock-breakout scenario but consistently underpredicted the observed X-ray emission. By employing a quasi-spherical outflow decelerated in a stratified environment, and incorporating a velocity-structured ejecta, self-absorption, and coasting-to-deceleration transitions, our model provides an improved multiwavelength fit. In particular, while we replicate radio observations well and better capture early X-ray features, we remain with problems in the late-time X-ray emission, especially for GRB 980425. The flux density remains underpredicted, similar to Barniol Duran et al. (2015), for both constant and wind-like media, with the constant-medium scenario being the most preferable.

Margutti et al. (2013) considered of the kinetic equivalent energy ($10^{46} \lesssim E \lesssim 10^{53}$ erg) and the profile of velocity ($10^{-2} \lesssim \Gamma\beta \lesssim 30$) distribution of the ejected material from ordinary Type Ib/c (Berger et al. 2003b; Soderberg et al. 2006a, 2008, 2010b,a; Sanders et al. 2012; Cano 2013; Milisavljevic et al. 2013; Mazzali et al. 2013; Kamble et al. 2013), from sub-energetic bursts (Berger et al. 2003a; Soderberg et al. 2006b; Cano 2013), from Relativistic SN 2009bb (Soderberg et al. 2010a; Cano 2013), and from classical bursts (Berger et al. 2003b; Frail et al. 2006; Chandra et al. 2008; Cano 2013; Fraija 2015; Fraija et al. 2016a, 2017b). Our sample of LL GRBs belongs to the sub-energetic bursts with similar values.

Starling et al. (2008) analysed a sample of 10 GRBs. They showed that four sources were consistent with a wind-like medium, while three were not. However, these last three were not necessarily well-fit by a constant medium, but rather with a stratification index $0 \leq k \leq 1$. Curran et al. (2009) constrained parameters for 10 GRBs by analysing their optical and X-ray light curves. They found that two of their GRBs were consistent with both $k = 0$ and $k = 2$, two only with $k = 0$ and two only with $k = 2$. Therefore, they concluded that the circumburst environments may be drawn from either of the two possibilities and they also discussed the possibility that $k \neq 0$ or 2. Schulze et al. (2011) assembled a sample of 27 Swift-detected GRBs (including one short GRB) and made observations about the density profiles of their environments using the observed X-ray and optical afterglow emission. They determined that out of their sample, 18 GRBs are consistent with environments that are homogeneous, while 6 GRBs are consistent with wind-like media. Aksulu et al. (2022) used Bayesian inference to infer the best-fit parameters for a sample of 22 long GRBs and 4 short GRBs. They considered both a $k = 0$ and a $k = 2$ model and found that there is approximately an even split between homogeneous and wind-like environments for the case of long GRBs.

Based on the jet break observed in the radio and optical bands of GRB 130603B, Fong et al. (2014) suggested a transition in the afterglow emission. The authors reported the best-fit value of the inferred jet opening angle was in the range of $\approx 4^\circ - 8^\circ$, which corresponded to a beaming-corrected kinetic energy in the range of $E \approx (0.1 - 1.6) \times 10^{49}$ erg. Fong et al. (2014) also reported a constant-density value of $n = 5 \times 10^{-3} - 30 \text{ cm}^{-3}$ from uncertainty of the self-absorption frequency in the standard synchrotron model. On the other hand, Hotokezaka & Piran (2015) were able to fit the radio light curves with $n = 1.0 \text{ cm}^{-3}$ and the microphysical parameters $\varepsilon_e = 0.2$, $\varepsilon_B = 8 \times 10^{-3}$. However, the possible range of the circumburst density spans several orders of magnitude, so with this in mind, Pandey et al. (2019) were able to fit light curves from microwaves to X-rays with the parameter values of $n \approx 0.004 \text{ cm}^{-3}$, $\varepsilon_e \approx 0.07$, $\varepsilon_B \approx 0.03$. For GRB 150101B, Fong et al. (2016) used the X-ray afterglow observations to constrain the circumburst density to $(0.8 - 4) \times 10^{-5} \text{ cm}^{-3}$ for $\varepsilon_B = 0.01 - 0.1$. More recently, Fraija et al. (2020a) were able to fit the X-ray light curve with an ISM model with $n \approx 10^{-2} \text{ cm}^{-3}$ for the microphysical parameters $\varepsilon_B \approx 10^{-2}$, $\varepsilon_e \approx 10^{-1}$, and with a stellar wind model with $A_{\text{st}} \approx 10^{-1}$ for $\varepsilon_B \approx 6 \times 10^{-2}$, $\varepsilon_e \approx 0.9 \times 10^{-1}$.

Fong et al. (2014) modeled the afterglow of short GRB 130603B using a standard synchrotron scenario from a collimated jet in a uniform medium. While they achieved good fits to the radio and optical data, their model significantly underpredicted the late-time X-ray emission. In contrast, our quasi-spherical outflow model, which accounts for stratified environments, velocity-structured ejecta, and self-absorption, successfully reproduces the multiwavelength observations, including the X-ray excess.

3.3 A burst sample reported in Swift satellite data base

It was unexpected to discover a GW event GW170817 at a close distance of ≈ 40 Mpc (Abbott et al. 2017a,b). A limited population of feeble gamma-ray transients following NS mergers was uncovered. GW170817 was linked to the faint and early gamma-ray emission of GRB 170817A (Goldstein et al. 2017; Savchenko et al. 2017) and the kilonova AT2017gfo (Coulter et al. 2017), which had an initial intense optical emission with an absolute magnitude of around -16 mag, 12 hours after the NS merger. This was followed by a very late multiwavelength afterglow, reaching its peak at ≈ 150 days after this merger (Troja et al. 2017; Kasliwal et al. 2017; Lamb & Kobayashi 2018; Resmi et al. 2018; Margutti et al. 2017; Lazzati et al. 2017; Gottlieb et al. 2018b; Fraija et al. 2019c; Gottlieb et al. 2018b; Fraija et al. 2019a).

Dichiara et al. (2020) conducted a methodical search in the Swift database spanning 14 years to find neighboring sGRBs like GRB 170817A. Four possible prospects, GRB 050906, GRB 070810B, GRB 080121, and GRB 100216A, were discovered within a range of 100 to 200 Mpc. They employed these potential sources to restrict the features of X-ray counterparts of the merging of two neutron stars, and calculated optical upper bounds for the beginning of a "blue" kilonova, suggesting a small quantity of lanthanide-deficient material.

3.3.1 Multi-band observations

We present the multi-band observations of the closest short bursts detected by Swift satellite.

3.3.1.1 GRB 050906 GRB 050906 triggered the Burst Alert Telescope (BAT) on board the Swift satellite at 2005 September 5 10:32:18 UTC with a reported location of R.A. = $03^{\text{h}}31^{\text{m}}13^{\text{s}}$, Dec = $-14^{\circ}37'30''$ (J2000) with a positional accuracy of 3' (Krimm et al. 2005). The light curve showed an excess in the 25-100 keV energy range. The duration and the observed fluence in the energy range of 15 - 150 keV were 128 ± 16 ms and $(5.9 \pm 3.2) \times 10^{-8}$ erg cm $^{-2}$, respectively (Parsons et al. 2005). Details of the deep optical and infrared observations collected with Swift are reported in Levan et al. (2008). According to the authors, neither X-ray nor optical/IR afterglow was discovered to deep limits.

3.3.1.2 GRB 070810B GRB 070810B triggered Swift BAT at 2007 August 10 15:19:17 UTC with a reported location of R.A. = $00^{\text{h}}35^{\text{m}}46^{\text{s}}$, Dec = $+08^{\circ}50'07''$ (J2000) with a positional accuracy of 3' (Marshall et al. 2007). Details of the follow-up observations carried out by the KANATA 1.5-m telescope, the Xinlong TNT 80 cm telescope, the 2-m Faulkes Telescope South, the Shajn 2.6 m telescope and the Keck I telescope (HST) are summarized in Bartos et al. (2019). Only the Shajn telescope detected a source inside the error box of GRB 070810B (Rumyantsev et al. 2007).

3.3.1.3 GRB 080121 GRB 080121 triggered Swift BAT at 2008 January 21 21:29:55 UTC with a reported location of R.A. = $09^{\text{h}}08^{\text{m}}56^{\text{s}}$, Dec = $+41^{\circ}50'29''$ (J2000) with a positional accuracy of 3'. The duration and the observed fluence in the 15-150 keV energy range were $T_{90} = 0.7 \pm 0.2$ s and $(3 \pm 2) \times 10^{-8}$ erg cm $^{-2}$ s $^{-1}$, respectively (Cummings & Palmer 2008). Follow-up observation were carried out 2.3 days after the burst using UVOT and XRT instruments, but neither X-ray afterglow candidate nor sources were found within the BAT error circle (Cucchiara & Schady 2008; Troja & Burrows 2008). Two galaxies were present within the BAT error circle, which would associate a redshift of $z \sim 0.046$ to GRB 080121, but the isotropic energy released would be several orders of magnitude less than in typical short-hard bursts (Perley et al. 2008).

3.3.1.4 GRB 100216A GRB 100216A triggered Swift BAT and Gamma-ray Burst Monitor (GBM) aboard the Fermi spacecraft at 2010 February 16 10:07:00 UTC with a reported location of R.A. = $10^{\text{h}}17^{\text{m}}03.2^{\text{s}}$, Dec = $+35^{\circ}31'27.5''$ (J2000) with a positional accuracy of 3'. The duration and the observed fluence of the single peak in the energy range of 15 - 350 keV were 0.3 s and $(4.7 \pm 3) \times 10^{-8}$ erg cm $^{-2}$, respectively (Cummings et al. 2010). Follow-up observations were conducted by XRT and UVOT from 214.4 ks to 249.2 ks after the BAT trigger. No fading source was detected within the observation, but a source thought to be 1RXS J101702.9+353404 was identified within the error circle (Rowlinson et al. 2010; Siegel & Rowlinson 2010).

3.3.2 Analysis and Description

Figure 9 presents the parameter space of rejected values of $(\varepsilon_B, \varepsilon_e, \beta)$ for GRB 050906, 080121 and 100216A. The other parameters of the model have been fixed to $n = 1 \text{ cm}^{-3}$, $E = 10^{50} \text{ erg}$, $\alpha_s = 2$ and $p = 2.2$ for all GRBs under consideration. Here, we define rejection as a set of parameters for which the flux overcomes the observational upper limits. Regions without color represent that any value of β is allowed and remains below the upper limits. On the other hand, areas of a particular color mean that any values larger than the corresponding β are rejected. The constraints are the most stringent in the GRB 050906 (left panel). A broad region of the $(\varepsilon_e, \varepsilon_B)$ space is colored, indicating that for a wide range of microphysical parameters, only sub-relativistic low values of β are compatible with the observational limits, namely $\beta \lesssim 0.7$. Contrastingly, GRB 080121 (middle panel) shows the least constrained parameter space. The uncolored region dominates the plot, which means that for most values of ε_e and ε_B , the modeled flux remains below the upper limits of the observation regardless of β . Only the top right corner, which corresponds to the most significant possible microphysical parameters, showcases some limits. Still, the constraints are relatively weak with $\beta \lesssim 0.85$, which still agrees with a relativistic shock. Finally, GRB 100216A (right panel) presents a relatively unconstrained scenario. The colored region is also limited to the top right corner, suggesting that while some parameter combinations are excluded for higher β , the constraints are generally weaker than in GRB 050906. Compared to GRB 080121, smaller values of β are required. The panel associated with GRB 070810's parameter space is not shown because the upper limits do not constrain any parameter region.

4 NEW POINTS IN OUR APPROACH AND PREVIOUS STUDIES

The quasi-spherical materials in the short- and long-burst scenarios have been associated with the cocoon (Nagakura et al. 2014; Murguia-Berthier et al. 2014; Lazzati et al. 2017, 2018; Nakar & Piran 2017; Gottlieb et al. 2018a) and shock breakout materials (Davies et al. 1994; Nakamura & Shigeyama 2006; Dessart et al. 2009; Balberg & Loeb 2011; Margutti et al. 2013; Nagakura et al. 2014; Kyutoku et al. 2014; Barniol Duran et al. 2015; Metzger et al. 2015; Förster et al. 2018; Fraija et al. 2019a; Haynie & Piro 2021; Goldberg et al. 2022). Nagakura et al. (2014) and Murguia-Berthier et al. (2014) derived the parameter space of Lorentz factor, duration and kinetic luminosity for short GRB production. Murguia-Berthier et al. (2014) concluded that if the jet successfully penetrates the neutrino-driven wind, the energy contained in the cocoon may enhance the precursor. They found that the cocoon material could be ejected with Lorentz factors in the $\Gamma \sim 2 - 3$ range. Nakar & Piran (2017) explored cocoon scenarios with Lorentz factors around ~ 10 . The shock breakout is traditionally expected to be a brief event lasting hours. However, Förster et al. (2018) analyzed observations of 26 supernovae and presented evidence that the shock breakout is significantly delayed and extended due to dense circumstellar material surrounding the star in most SNe II. This material causes the shock to emerge gradually over several days, rather than hours. Similarly, Haynie & Piro (2021) also explored how dense circumstellar material around a star influences the shock breakout during a supernova event. The authors also concluded that the interaction with a dense circumstellar material can extend the shock breakout's duration and increase its brightness. They focused on the case of the supernova PS1-13arp, which exhibited an early UV excess indicative of such an interaction. Goldberg et al. (2022) utilized Athena++ to conduct 3D Radiation-Hydrodynamic simulations of the radiative breakout of a shock wave in the outermost layer of a red supergiant (RSG) that has undergone core collapse and is expected to evolve into a Type IIP supernova. Balberg & Loeb (2011) proposed a simple scenario to estimate the conditions during shock breakout in a stellar wind. This model was based on the observable parameters in the X-ray flash light curve, such as the total

X-ray energy and the diffusion time after the maximum flux, and provided relationships for the radius and velocity of the shock at the moment of breakout. The derivation required the self-similar solution for the structure of a forward-reverse shock that is anticipated when ejecta moves through a pre-existing wind at significant distances from the surface of the progenitor. [Margutti et al. \(2013\)](#) conducted a spectral and temporal study of GRB 100316D using late-time radio and X-ray data. The results showed a mildly relativistic material moving with $\Gamma = 1.5 - 2$, and $\alpha_s \sim 2.4$, indicating that the progenitor of the GRB was likely the formation of a magnetar with extremely rapid rotation. [Kyutoku et al. \(2014\)](#) considered an ultrarelativistic shock breakout ejected from a binary NS and decelerated by a constant circumstellar medium. They estimated the radio, optical, and X-ray fluxes in timescales from seconds to days after the trigger time. [Barniol Duran et al. \(2015\)](#) proposed that the prompt and afterglow emission of some long IIGRBs (GRB 980425, 031203, 060218, 100316D) could be described by the deceleration of the relativistic shock breakout material in a stellar wind and ISM. The authors observed differences in X-ray fluxes, suggesting unconsidered environmental complexity. [Metzger et al. \(2015\)](#) and [Hotokezaka & Piran \(2015\)](#) proposed a shock breakout material from a binary NS and estimated the radio fluxes on timescale of days to months. [Frajia et al. \(2019a\)](#) derived the synchrotron light curves of a shock-breakout material when it decelerates in a uniform medium and also applied this phenomenological model to describe the multiwavelength afterglow emission up to a pair of weeks of GRB 170817A.

Previous studies of GRB afterglows often assume a circumburst environment modeled as a constant density medium ($k = 0$) or a stellar wind ($k = 2$), with fixed microphysical parameters and a standard electron spectral index ($p > 2$). These assumptions face challenges in explaining the stratified density profiles inferred from observations of GRB-SNe systems (e.g., see [Berger et al. 2013; Izzo et al. 2019; Frajia et al. 2020b](#)). In some cases, such as GRBs 980425 and 060218, the multiwavelength observations have been partially described, and more than one electron population is required. For instance, [Barniol Duran et al. \(2015\)](#) considered a wind shock-breakout model to fit the radio data of GRB 980425. However, the same afterglow model used to fit the radio led to a very low X-ray flux and soft X-ray spectrum, contrasting with the observations. However, the authors showed that the model can simultaneously explain the radio and X-ray observations with a modification introducing two power-law electron distributions; a distribution with $p = 2.8$ for the radio-emitting electrons and $p = 2.1$ for the X-ray-emitting ones. [Barniol Duran et al. \(2015\)](#) explained the prompt emission of GRB 060218 as arising from a mildly relativistic shock breakout, and its radio afterglow from the interaction between ejecta and the surrounding wind medium. They found that the shock remained in a coasting phase, with a Lorentz factor close to 1.3, until deceleration occurred around 200 days. While they could fit the radio data with this model, the predicted X-ray afterglow significantly underpredicted the observed X-ray flux. The authors suggested that the X-ray and radio emissions might originate from different electron populations or emission processes. The authors found good agreement in the radio bands for a wind medium with $A_{st} = 1$, $\varepsilon_B = 1.5 \times 10^{-5}$, $\varepsilon_e = 0.2$, and $p = 2.6$. To overcome this limitation, we have systematically generalized the afterglow model to $0 \leq k < 3$, allowing for analyzing environments beyond ISM or wind, such as those predicted for merger ejecta or progenitors with non-steady mass loss ([Ramirez-Ruiz et al. 2005; Moriya & Tominaga 2012](#)). Additionally, we have broadened the synchrotron spectra to encompass the amount of electrons accelerated by the shock front and the self-absorption regime, which is essential for modeling early radio emission ([Urata et al. 2019](#)). We have also unified the relativistic and sub-relativistic regimes, facilitating continuous modeling from prompt cocoon or breakout material to late-time emission.

5 CONCLUSION

We have extended the analytical synchrotron afterglow scenario of the quasi-spherical material previously utilized to characterize the early X-ray, optical and radio afterglow observations from GRB 170817A ([Frajia et al. 2019c](#)). Binary compact objects are predicted to have a uniform-density medium ($k = 0$), but massive stars with varying mass-loss evolutions (\dot{M} or v_w) towards the end of their lifetimes are expected to consist of a stratified medium ($0 \leq k < 3$; [Ramirez-Ruiz et al. 2005; van Marle et al. 2006](#)). In the current model, we have generalized and derived the light curves to a stratified environment with a density profile $\propto r^{-k}$ with $0 \leq k < 3$, including the coasting phase, the self-absorption regime and considering the possibility that not all electrons are accelerated by the shock front, but just a fraction of them.

We calculated synchrotron light curves for both fast- and slow-cooling scenarios during the coasting and deceleration phases. In the coasting phase, we considered velocities between $0.07 < \beta < 0.8$, and for the deceleration phase, we used a power-law velocity distribution $\propto \beta^{-\alpha_s}$ with $3 < \alpha_s < 5.2$ for a source located at 100 Mpc. For typical parameter values of GRB afterglows, we presented synchrotron light curves for radio at 6 GHz, optical at 1 eV, and X-rays at 1 keV. The majority of light curves peak in a matter of months or years. On the other hand, the light curve peak might happen in a matter of hours, days or weeks if the quasi-spherical outflow is extremely energetic or slows down in a dense medium. We showed that density parameter variations are more easily observed (i) in radio rather than X-ray light curves, (ii) in stratified rather than uniform-density media, and (iii) for higher values of α_s . Hence, the transition from a stellar-wind to a uniform-density medium is more noticeable in radio bands.

We showed that a light curve flattening or rebrightening occurs when nonrelativistic material decelerates in a uniform-density medium; rebrightening is less noticeable when decelerating in a stratified medium. Therefore, deceleration of nonrelativistic material from a binary compact object merger is indicated by a flattening or rebrightening over months to years in conjunction with GW detection. On the other hand, a steadily declining flux over several months to years might signify a slowdown of ejecta from the death of a massive star with varying mass loss at the end of its life. We calculated the expected gamma-ray, X-ray, optical, and radio fluxes from synchrotron emission of electrons in forward shocks. These electromagnetic signatures over different timescales and frequencies resemble those around SNe in a uniform-density medium and coincide with GW detections.

We have applied this analytical model to interpret a sample of IIGRBs (GRB 980425, 031203, 060218, 100316D, 130603B, 150101B and 171205A), the Swift-BAT database with sGRBs located between 100 and 200 Mpc (GRB 050906, 070810B, 080121, 080121 and 100216A). We have used the multiwavelength observations and upper limits to model and constrain the parameters (\tilde{E} , A_{st} , Γ_0 , ε_B , ε_e , p , α_s , θ_c) in our analytical afterglow model through MCMC simulations. As expected, we have found that all of the results are consistent with sub-energetic GRBs. The large values of half-opening angles found with our MCMC simulations agree with the multiwavelength observations which show no indication of late, steep decays over a time scale of weeks. We propose that some GRBs with no indication of late steep decays in a time scale of days could be associated with large half-opening angles.

The Fermi GBM initially observed GRB 170817A on August 17, 2017 at 12:41:06. Just before the GBM trigger, the LIGO Scientific Collaboration and the Virgo Collaboration announced the detection of a GW candidate (GW170817) that matched the position of GRB 170817A ([Connaughton et al. 2017; Abbott et al. 2017a,b](#)). The progenitor of GRB 170817A was immediately linked to the merging of two neutron stars, marking the initial observation of GWs ([Abbott et al. 2017a,b](#)). GRB 170817A was promptly followed by a comprehensive observing effort that included radio, optical, and X-ray wavelengths (e.g., see [Troja et al. 2017; Abbott et al. 2017b](#), and references therein). The non-thermal spectrum collected over the first approximately 900 days following this merger was modelled by synchrotron radiation emitted by an off-axis structure jet (e.g., see [Troja et al. 2017; Kasliwal et al. 2017; Lamb & Kobayashi 2018; Resmi et al. 2018; Margutti et al. 2017; Lazzati et al. 2017; Gottlieb et al. 2018b; Frajia et al. 2019c,a](#)). [Hajela et al. \(2022\)](#) examined the most recent X-ray and radio data of GRB 170817A, which were obtained using CXO, VLA and the MeerKAT around 3.3 years after the merger. [Hajela et al. \(2022\)](#) noticed and reported evidence of an unexpected X-ray emission component, which did not align with the synchrotron off-axis afterglow hypothesis in a constant-density medium. This X-ray excess would be a candidate to be described with the quasi-spherical outflow model in the sub-relativistic regime.

ACKNOWLEDGEMENTS

We express our sincere gratitude to the anonymous referee for their thorough review of the paper and valuable suggestions that enhanced the clarity of the manuscript. We greatly appreciate the useful discussions with Rodolfo Barniol-Duran and Tanmoy Laskar. NF is grateful to UNAM-DGAPA-PAPIIT for the funding provided by grant IN112525. BBK is supported by IBS under the project code IBS-R018-D3. AG was supported by Universidad Nacional Autónoma de México Postdoctoral Program (POSDOC).

DATA AVAILABILITY

No new data were generated or analysed in support of this research.

REFERENCES

Abbott B. P., Abbott R., Abbott T. D., et al., 2017a, *Phys. Rev. Lett.*, **119**, 161101
 Abbott B. P., Abbott R., Abbott T. D., et al., 2017b, *The Astrophysical Journal Letters*, **848**, L12
 Aksulu M. D., Wijers R. A. M. J., van Eerten H. J., et al., 2022, *MNRAS*, **511**, 2848
 Bailyn C., Buxton M., Cobb B., et al., 2003, GRB Coordinates Network, **2463**, 1
 Balberg S., Loeb A., 2011, *MNRAS*, **414**, 1715
 Band D., Matteson J., Ford L., et al., 1993, *ApJ*, **413**, 281
 Barniol Duran R., Nakar E., Piran T., et al., 2015, *MNRAS*, **448**, 417
 Barthelmy S. D., Cannizzo J. K., Gehrels N., et al., 2005, *ApJ*, **635**, L133
 Barthelmy S. D., Baumgartner W. H., Cummings J. R., et al., 2013, GRB Coordinates Network, **14741**, 1
 Barthelmy S. D., Cummings J. R., D'Elia V., et al., 2017, GRB Coordinates Network, **22184**, 1
 Bartos I., Lee K. H., Corsi A., et al., 2019, *MNRAS*, **485**, 4150
 Berger E., Kulkarni S. R., Pooley G., et al., 2003a, *Nature*, **426**, 154
 Berger E., Kulkarni S. R., Frail D. A., et al., 2003b, *ApJ*, **599**, 408
 Berger E., Fong W., Chornock R., 2013, *ApJ*, **774**, L23
 Blandford R. D., McKee C. F., 1976, *Physics of Fluids*, **19**, 1130
 Bromberg O., Nakar E., Piran T., 2011, *ApJ*, **739**, L55
 Burns E., Veres P., Connaughton V., et al., 2018, *ApJ*, **863**, L34
 Campana S., et al. 2006, *Nature*, **442**, 1008
 Cano Z., 2013, *MNRAS*, **434**, 1098
 Cano Z., Bersier D., Guidorzi C., et al., 2011, *ApJ*, **740**, 41
 Cano Z., Izzo L., de Ugarte Postigo A., et al., 2017a, *A&A*, **605**, A107
 Cano Z., Wang S.-Q., Dai Z.-G., et al., 2017b, *Advances in Astronomy*, **2017**, 8929054
 Chandra P., Cenko S. B., Frail D. A., et al., 2008, *ApJ*, **683**, 924
 Changsu Choi M. I., 2017, GRB Coordinates Network, **22188**, 1
 Chornock R., Berger E., Levesque E. M., et al., 2010, *arXiv e-prints*, p. arXiv:1004.2262
 Cobb B. E., 2017, GRB Coordinates Network, **22192**, 1
 Colgate S. A., 1974, *ApJ*, **187**, 333
 Connaughton V., GBM-LIGO Group Blackburn L., et al., 2017, GRB Coordinates Network, **21506**, 1
 Coulter D. A., Foley R. J., Kilpatrick C. D., Drout M. R., et al., 2017, *Science*, **358**, 1556
 Cucchiara A., Schady P., 2008, GRB Coordinates Network, **7217**
 Cucchiara A., Prochaska J. X., Perley D., et al., 2013, *ApJ*, **777**, 94
 Cummings J. R., Palmer M., 2008, GRB Coordinates Network, **7209**
 Cummings J. R., Barthelmy S. D., Fox D. B., et al., 2010, GRB Coordinates Network, **10428**
 Cummings J. R., Gropp M., Page K. L., et al., 2015, *The Astronomer's Telegram*, **6871**, 1
 Curran P. A., Starling R. L. C., van der Horst A. J., et al., 2009, *MNRAS*, **395**, 580
 Cusumano G., Barthelmy S., Gehrels N., et al., 2006, GRB Coordinates Network, **4775**, 1
 D'Elia V., D'Ai A., Lien A. Y., et al., 2017, GRB Coordinates Network, **22177**, 1
 D'Elia V., Campana S., D'Ai A., et al., 2018, *A&A*, **619**, A66
 Dai Z. G., Wu X. F., 2003, *ApJ*, **591**, L21
 Daigne F., Mochkovitch R., 2007, *A&A*, **465**, 1
 Davies M. B., Benz W., Piran T., et al., 1994, *ApJ*, **431**, 742
 Dessart L., Ott C. D., Burrows A., et al., 2009, *ApJ*, **690**, 1681
 Dichiara S., Troja E., O'Connor B., et al., 2020, *MNRAS*, **492**, 5011
 Duncan R. C., Thompson C., 1992, *ApJ*, **392**, L9
 Emery S. W. K., D'Elia V., 2017, GRB Coordinates Network, **22181**, 1
 Ensman L., Burrows A., 1992, *ApJ*, **393**, 742
 Evans P. A., Goad M. R., Osborne J. P., et al., 2013, GRB Coordinates Network, **14739**, 1
 Falk S. W., 1978, *ApJ*, **225**, L133
 Fan Y., Piran T., 2006, *MNRAS*, **369**, 197
 Fan Y.-Z., Zhang B.-B., Xu D., et al., 2011, *ApJ*, **726**, 32
 Foley R. J., Chornock R., Fong W., et al., 2013, GRB Coordinates Network, **14745**, 1
 Fong W., Zauderer B. A., Berger E., 2013a, GRB Coordinates Network, **14751**, 1
 Fong W., Migliori G., Margutti R., et al., 2013b, GRB Coordinates Network, **14922**, 1

Fong W., Berger E., Metzger B. D., et al., 2014, [ApJ](#), **780**, 118
 Fong W., Berger E., Margutti R., et al., 2015, [ApJ](#), **815**, 102
 Fong W., Margutti R., Chornock R., et al., 2016, [ApJ](#), **833**, 151
 Förster F., Moriya T. J., Maureira J. C., et al., 2018, [Nature Astronomy](#), **2**, 808
 Fraija N., 2015, [ApJ](#), **804**, 105
 Fraija N., Lee W., Veres P., 2016a, [ApJ](#), **818**, 190
 Fraija N., Lee W. H., Veres P., et al., 2016b, [ApJ](#), **831**, 22
 Fraija N., Veres P., Zhang B. B., et al., 2017a, [ApJ](#), **848**, 15
 Fraija N., Lee W. H., Araya M., et al., 2017b, [ApJ](#), **848**, 94
 Fraija N., Pedreira A. C. C. d. E. S., Veres P., 2019a, [ApJ](#), **871**, 200
 Fraija N., Dichiara S., Pedreira A. C. C. d. E. S., et al., 2019b, [ApJ](#), **879**, L26
 Fraija N., Lopez-Camara D., Pedreira A. C. C. d. E. S., et al., 2019c, [ApJ](#), **884**, 71
 Fraija N., De Colle F., Veres P., et al., 2020a, [ApJ](#), **896**, 25
 Fraija N., Laskar T., Dichiara S., et al., 2020b, [ApJ](#), **905**, 112
 Fraija N., Kamenetskaia B. B., Dainotti M. G., et al., 2021a, [ApJ](#), **907**, 78
 Fraija N., Veres P., Beniamini P., et al., 2021b, [ApJ](#), **918**, 12
 Frail D. A., 2003, GRB Coordinates Network, **2473**, 1
 Frail D. A., Kulkarni S. R., Sari R., et al., 2001, [ApJ](#), **562**, L55
 Frail D. A., Cameron P. B., Kasliwal M., et al., 2006, [ApJ](#), **646**, L99
 Frederiks D., Golenetskii S., Aptekar R., et al., 2017, GRB Coordinates Network, **22227**, 1
 Galama T. J., Vreeswijk P. M., van Paradijs J., et al., 1998, [Nature](#), **395**, 670
 Giblin T. W., van Paradijs J., Kouveliotou C., et al., 1999, [ApJ](#), **524**, L47
 Goldberg J. A., Jiang Y.-F., Bildsten L., 2022, [ApJ](#), **933**, 164
 Goldstein A., Veres P., Burns E., et al., 2017, [ApJ](#), **848**, L14
 Gottlieb O., Nakar E., Piran T., 2018a, [MNRAS](#), **473**, 576
 Gottlieb O., Nakar E., Piran T., et al., 2018b, [MNRAS](#), **479**, 588
 Gotz D., Mereghetti S., Beck M., et al., 2003, GRB Coordinates Network, **2459**, 1
 Hajela A., Margutti R., Bright J. S., et al., 2022, [ApJ](#), **927**, L17
 Haynie A., Piro A. L., 2021, [ApJ](#), **910**, 128
 Hjorth J., 2013, [Philosophical Transactions of the Royal Society of London Series A](#), **371**, 20120275
 Hotokezaka K., Piran T., 2015, [MNRAS](#), **450**, 1430
 Huang Y. F., Dai Z. G., Lu T., 1999, [MNRAS](#), **309**, 513
 Imshennik V. S., Nadezhin D. K., Utrobin V. P., 1981, [Ap&SS](#), **78**, 105
 Irwin C. M., Chevalier R. A., 2016, [MNRAS](#), **460**, 1680
 Izzo L., Kann D. A., Fynbo J. P. U., et al., 2017a, GRB Coordinates Network, **22178**, 1
 Izzo L., Selsing J., Japelj J., et al., 2017b, GRB Coordinates Network, **22180**, 1
 Izzo L., de Ugarte Postigo A., Maeda K., et al., 2019, [Nature](#), **565**, 324
 Izzo L., Auchettl K., Hjorth J., et al., 2020, [A&A](#), **639**, L11
 Jin Z. P., Xu D., Covino S., et al., 2009, [MNRAS](#), **400**, 1829
 Jin Z.-P., Li X., Wang H., et al., 2018, [ApJ](#), **857**, 128
 Kamble A., Resmi L., Misra K., 2007, [ApJ](#), **664**, L5
 Kamble A., Soderberg A. M., Chomiuk L., et al., 2013, [arXiv e-prints](#), p. arXiv:1309.3573
 Kasliwal M. M., Nakar E., Singer L. P., et al., 2017, [Science](#), **358**, 1559
 Katz B., Budnik R., Waxman E., 2010, [ApJ](#), **716**, 781
 Katz B., Sapir N., Waxman E., 2012, [ApJ](#), **747**, 147
 Kennea J. A., Burrows D. N., Cusumano G., et al., 2006, GRB Coordinates Network, **4776**, 1
 Kennea J. A., Stroh M. C., Burrows D. N., et al., 2013, GRB Coordinates Network, **14749**, 1
 Kennea J. A., Sbarufatti B., Burrows D. N., et al., 2017, GRB Coordinates Network, **22183**, 1
 Kippen R. M., the BATSE GRB team 1998, GRB Coordinates Network, **67**, 1
 Klein R. I., Chevalier R. A., 1978, [ApJ](#), **223**, L109
 Kouveliotou C., Meegan C. A., Fishman G. J., et al., 1993, [The Astrophysical Journal](#), **413**, L101
 Kouveliotou C., Woosley S. E., Patel S. K., et al., 2004, [ApJ](#), **608**, 872
 Kouveliotou C., Granot J., Racusin J. L., et al., 2013, [ApJ](#), **779**, L1
 Krimm H., La Parola V., de Pasquale M., et al., 2005, GRB Coordinates Network, **3926**, 1
 Kulkarni S. R., Frail D. A., Wieringa M. H., et al., 1998, [Nature](#), **395**, 663
 Kumar P., Narayan R., Johnson J. L., 2008, [Science](#), **321**, 376
 Kyutoku K., Ioka K., Shibata M., 2014, [MNRAS](#), **437**, L6
 Lamb G. P., Kobayashi S., 2018, [MNRAS](#), **478**, 733
 Lamb D. Q., Donaghy T. Q., Graziani C., 2005, [ApJ](#), **620**, 355
 Lazzati D., López-Cámarra D., Cantiello M., et al., 2017, [ApJ](#), **848**, L6
 Lazzati D., Perna R., Morsany B. J., Lopez-Camara D., et al., 2018, [Phys. Rev. Lett.](#), **120**, 241103
 Levan A. J., Tanvir N. R., Jakobsson P., et al., 2008, [MNRAS](#), **384**, 541
 Li Z.-Y., Chevalier R. A., 1999, [ApJ](#), **526**, 716
 Li L., Wang X.-G., Zheng W., et al., 2020, [ApJ](#), **900**, 176
 Liang E.-W., Li L., Gao H., et al., 2013, [ApJ](#), **774**, 13
 Lu-Lu Z., Jia R., Xiao-Li H., et al., 2021, arXiv e-prints, p. arXiv:2106.03466
 Maity B., Chandra P., 2021, [ApJ](#), **907**, 60
 Mao J., Ding X., Bai J. M., 2017, GRB Coordinates Network, **22186**, 1

Margutti R., Chincarini G., Covino S., et al., 2007, [A&A](#), **474**, 815

Margutti R., Soderberg A. M., Wieringa M. H., et al., 2013, [ApJ](#), **778**, 18

Margutti R., Berger E., Fong W., et al., 2017, [ApJ](#), **848**, L20

Marshall F., Immel S., Cusumano G., 2006, GRB Coordinates Network, [4779](#), 1

Marshall F. E., Brown P. J., Cummings J. R., et al., 2007, GRB Coordinates Network, [6743](#), 1

Mazets E., Golenetskii S., Il'Inskii V., et al., 1981, *Astrophysics and Space Science*, **80**, 3

Mazzali P. A., Walker E. S., Pian E., et al., 2013, [MNRAS](#), **432**, 2463

Melandri A., Baumgartner W. H., Burrows D. N., et al., 2013, GRB Coordinates Network, [14735](#), 1

Melandri A., D'Avanzo P., di Fabrizio L., et al., 2017, GRB Coordinates Network, [22189](#), 1

Metzger B. D., Giannios D., Thompson T. A., Bucciantini N., et al., 2011, [MNRAS](#), **413**, 2031

Metzger B. D., Bauswein A., Goriely S., et al., 2015, [MNRAS](#), **446**, 1115

Milisavljevic D., Soderberg A. M., Margutti R., et al., 2013, [ApJ](#), **770**, L38

Mirabal N., Halpern J. P., 2006, GRB Coordinates Network, [4792](#), 1

Mizuta A., Ioka K., 2013, [ApJ](#), **777**, 162

Moriya T. J., Tominaga N., 2012, [ApJ](#), **747**, 118

Murguia-Berthier A., Montes G., Ramirez-Ruiz E., et al., 2014, [ApJ](#), **788**, L8

Nagakura H., Hotokezaka K., Sekiguchi Y., et al., 2014, [ApJ](#), **784**, L28

Nakamura K., Shigeyama T., 2006, [ApJ](#), **645**, 431

Nakar E., Piran T., 2017, [ApJ](#), **834**, 28

Nakar E., Sari R., 2010, [ApJ](#), **725**, 904

Nakar E., Sari R., 2012, [ApJ](#), **747**, 88

Narayan R., Paczynski B., Piran T., 1992, [ApJ](#), **395**, L83

Paczynski B., 1998, [ApJ](#), **494**, L45

Panaiteescu A., Mészáros P., 1998, [ApJ](#), **501**, 772

Pandey S. B., Hu Y., Castro-Tirado A. J., et al., 2019, [MNRAS](#), **485**, 5294

Parsons A., Sarazin C., Barbier L., et al., 2005, GRB Coordinates Network, [3935](#), 1

Pe'er A., Mészáros P., Rees M. J., 2006, [ApJ](#), **652**, 482

Perley D. A., Foley R. J., Bloom J. S., 2008, GRB Coordinates Network, [7210](#)

Pian E., Amati L., Antonelli L. A., et al., 2000, [ApJ](#), **536**, 778

Pian E., Giommi P., Amati L., et al., 2004, *Advances in Space Research*, **34**, 2711

Planck Collaboration Ade P. A. R., Aghanim N., Arnaud M., et al., 2016, [A&A](#), **594**, A13

Prochaska J. X., Bloom J. S., Chen H.-W., et al., 2004, [ApJ](#), **611**, 200

Ramirez-Ruiz E., Celotti A., Rees M. J., 2002, [MNRAS](#), **337**, 1349

Ramirez-Ruiz E., García-Segura G., Salmonson J. D., Pérez-Rendón B., 2005, [ApJ](#), **631**, 435

Resmi L., Schulze S., Ishwara-Chandra C. H., et al., 2018, [ApJ](#), **867**, 57

Rezzolla L., Kumar P., 2015, [ApJ](#), **802**, 95

Rowlinson A., Page K., Lyons N., 2010, GRB Coordinates Network, [10435](#)

Rumyantsev V., Biryukov V., Pozanenko A., 2007, GRB Coordinates Network, [6762](#), 1

Sakamoto T., Barthelmy S. D., Baumgartner W. H., et al., 2010, GRB Coordinates Network, [10511](#), 1

Sanders N. E., Soderberg A. M., Valenti S., et al., 2012, [ApJ](#), **756**, 184

Santana R., Barniol Duran R., Kumar P., 2014, [ApJ](#), **785**, 29

Santos-Lleo M., Calderon P., Gotz D., 2003, GRB Coordinates Network, [2464](#), 1

Sari R., Esin A. A., 2001, [ApJ](#), **548**, 787

Sari R., Mészáros P., 2000, [ApJ](#), **535**, L33

Sari R., Piran T., 1999, [A&AS](#), **138**, 537

Sari R., Piran T., Narayan R., 1998, [ApJ](#), **497**, L17

Sari R., Piran T., Halpern J. P., 1999, [ApJ](#), **519**, L17

Sato Y., Obayashi K., Yamazaki R., et al., 2021, [MNRAS](#), **504**, 5647

Savchenko V., Ferrigno C., Kuulkers E., et al., 2017, [ApJ](#), **848**, L15

Schulze S., Klose S., Björnsson G., et al., 2011, in McEnery J. E., Racusin J. L., Gehrels N., eds, American Institute of Physics Conference Series Vol. 1358, Gamma Ray Bursts 2010. AIP, pp 165–168, doi:10.1063/1.3621763

Schulze S., Malesani D., Cucchiara A., et al., 2014, [A&A](#), **566**, A102

Siegel M. H., Rowlinson A., 2010, GRB Coordinates Network, [10442](#)

Sironi L., Spitkovsky A., Arons J., 2013, [ApJ](#), **771**, 54

Soderberg A. M., Kulkarni S. R., Berger E., et al., 2004, [Nature](#), **430**, 648

Soderberg A. M., Kulkarni S. R., Nakar E., et al., 2006a, [Nature](#), **442**, 1014

Soderberg A. M., Nakar E., Berger E., et al., 2006b, [ApJ](#), **638**, 930

Soderberg A. M., Berger E., Page K. L., et al., 2008, [Nature](#), **453**, 469

Soderberg A. M., Chakraborti S., Pignata G., et al., 2010a, [Nature](#), **463**, 513

Soderberg A. M., Brunthaler A., Nakar E., et al., 2010b, [ApJ](#), **725**, 922

Soffitta P., Feroci M., Piro L., et al., 1998, IAU Circular, 6884, 1

Stamatikos M., Barthelmy S. D., Baumgartner W. H., et al., 2010, GRB Coordinates Network, [10496](#), 1

Starling R. L. C., van der Horst A. J., Rol E., et al., 2008, [ApJ](#), **672**, 433

Tan J. C., Matzner C. D., McKee C. F., 2001, [ApJ](#), **551**, 946

Tanvir N. R., Levan A. J., Fruchter A. S., et al., 2013, [Nature](#), **500**, 547

Thompson C., 1994, [MNRAS](#), **270**, 480

Thomsen B., Hjorth J., Watson D., et al., 2004, [A&A](#), **419**, L21

Tinney C., Stathakis R., Cannon R., et al., 1998, IAU Circular, 6896, 1

Troja E., Burrows D. N., 2008, GRB Coordinates Network, [7224](#)
 Troja E., Piro L., van Eerten H., et al., 2017, [Nature](#), **000**, 1
 Troja E., Ryan G., Piro L., et al., 2018, [Nature Communications](#), **9**, [4089](#)
 Urata Y., Toma K., Huang K., et al., 2019, [ApJ](#), **884**, [L58](#)
 Usov V. V., 1992, [Nature](#), **357**, [472](#)
 Valeev A., et al. 2019, GRB Coordinates Network, Circular Service, No. 25565, #1 (2019), [25565](#)
 Vergani S. D., D'Avanzo P., Levan A. J., et al., 2010, GRB Coordinates Network, [10512](#), [1](#)
 Wang X. Y., Dai Z. G., Lu T., 2000, [Monthly Notices of the Royal Astronomical Society](#), **319**, [1159](#)
 Wang X.-Y., He H.-N., Li Z., et al., 2010, [ApJ](#), **712**, [1232](#)
 Watson D., Hjorth J., Levan A., et al., 2004, [ApJ](#), **605**, [L101](#)
 Waxman E., Mészáros P., Campana S., 2007, [ApJ](#), **667**, [351](#)
 Weinberg S., 1972, [Gravitation and Cosmology](#)
 Wieringa M., Frail D. A., Kulkarni S. R., et al., 1998, GRB Coordinates Network, **63**
 Woosley S. E., 1993, [ApJ](#), **405**, [273](#)
 Woosley S. E., Bloom J. S., 2006, [ARA&A](#), **44**, [507](#)
 Yamazaki R., Toma K., Ioka K., et al., 2006, [MNRAS](#), **369**, [311](#)
 Yi S.-X., Wu X.-F., Dai Z.-G., 2013, [ApJ](#), **776**, [120](#)
 de Ugarte Postigo A., Thöne C. C., Rowlinson A., et al., 2014, [A&A](#), **563**, [A62](#)
 de Ugarte Postigo A., Izzo L., Kann D. A., et al., 2017, [The Astronomer's Telegram](#), **11038**, [1](#)
 van Marle A. J., Langer N., Achterberg A., García-Segura G., 2006, [A&A](#), **460**, [105](#)

Table 1. Evolution of the synchrotron light curves ($F_\nu \propto t^{-\alpha} \nu^{-\beta}$) from a cocoon/shock breakout material decelerated in a stratified environment

β	Coasting Phase		Deceleration Phase		Lateral Expansion
	Sub-relativistic	Relativistic	Sub-relativistic	Relativistic	
α	α	α	α	α	
$\nu_{a,3} < \nu_c < \nu_m$					
$\nu < \nu_{a,3}$	-2	$-(1+k)$	$-(1+k)$	$-\frac{5+\alpha_s+k(1+\alpha_s)}{\alpha_s+5-k}$	$-\frac{8+\alpha_s(1+k)}{\alpha_s+8-2k}$
$\nu_{a,3} < \nu < \nu_c$	$-\frac{1}{3}$	$\frac{6k-11}{3}$	$\frac{6k-11}{3(\alpha_s+5-k)}$	$-\frac{2(5-4k)+\alpha_s(11-6k)}{3(\alpha_s+8-2k)}$	$-\frac{18-11\alpha_s+6k(\alpha_s-1)}{3(\alpha_s+6-2k)}$
$\nu_c < \nu < \nu_m$	$\frac{1}{2}$	$\frac{3k-8}{4}$	$\frac{3k-8}{4(\alpha_s+5-k)}$	$-\frac{2(5-2k)+\alpha_s(8-3k)}{4(\alpha_s+8-2k)}$	$\frac{8(3-k)+\alpha_s(3k-8)}{4(\alpha_s+6-2k)}$
$\nu_m < \nu$	$\frac{p}{2}$	$\frac{k(2+p)-8}{4}$	$\frac{k(2+p)-8}{4(\alpha_s+5-k)}$	$\frac{30p+kp(\alpha_s-8)-8(\alpha_s+5)+2k(\alpha_s+6)}{4(\alpha_s+8-2k)}$	$\frac{p[24+k(\alpha_s-8)+2k(2+\alpha_s)]}{4(\alpha_s+6-2k)}$
$\nu_{a,1} < \nu_m < \nu_c$					
$\nu < \nu_{a,1}$	-2	-2	-2	$-\frac{2(\alpha_s+k-1)}{\alpha_s+5-k}$	$-\frac{2(\alpha_s+2)}{\alpha_s+8-2k}$
$\nu_{a,1} < \nu < \nu_m$	$-\frac{1}{3}$	$\frac{4k-9}{3}$	$\frac{4k-9}{3(\alpha_s+5-k)}$	$-\frac{3(8+3\alpha_s)-2k(2\alpha_s+5)}{3(\alpha_s+8-2k)}$	$-\frac{6(2-k)+\alpha_s(9-4k)}{3(\alpha_s+6-2k)}$
$\nu_m < \nu < \nu_c$	$\frac{p-1}{2}$	$\frac{k(5+p)-12}{4}$	$\frac{k(5+p)-12}{4(\alpha_s+5-k)}$	$\frac{6(5p-2\alpha_s-7)+k[16+p(\alpha_s-8)+5\alpha_s]}{4(\alpha_s+8-2k)}$	$\frac{12(2p-2-\alpha_s)+kp(\alpha_s-6)+5k(\alpha_s+2)}{4(\alpha_s+6-2k)}$
$\nu_c < \nu$	$\frac{p}{2}$	$\frac{k(2+p)-8}{4}$	$\frac{k(2+p)-8}{4(\alpha_s+5-k)}$	$\frac{30p+kp(\alpha_s-8)-8(\alpha_s+5)+2k(\alpha_s+6)}{4(\alpha_s+8-2k)}$	$\frac{8(3p-2-\alpha_s)+kp(\alpha_s-6)+2k(2+\alpha_s)}{4(\alpha_s+6-2k)}$
$\nu_m < \nu_{a,2} < \nu_c$					
$\nu < \nu_m$	-2	-2	-2	$-\frac{2(\alpha_s+k-1)}{\alpha_s+5-k}$	$-\frac{2(\alpha_s+2)}{\alpha_s+8-2k}$
$\nu_m < \nu < \nu_{a,2}$	$-\frac{5}{2}$	$-\frac{8+k}{4}$	$-\frac{8+k}{4}$	$-\frac{22+\alpha_s(8+k)}{4(\alpha_s+5-k)}$	$-\frac{8(\alpha_s+5)+k(\alpha_s-6)}{4(\alpha_s+8-2k)}$
$\nu_{a,2} < \nu < \nu_c$	$\frac{p-1}{2}$	$\frac{k(5+p)-12}{4}$	$\frac{k(5+p)-12}{4(\alpha_s+5-k)}$	$\frac{6(5p-2\alpha_s-7)+k[16+p(\alpha_s-8)+5\alpha_s]}{4(\alpha_s+8-2k)}$	$\frac{12(2p-2-\alpha_s)+kp(\alpha_s-6)+5k(\alpha_s+2)}{4(\alpha_s+6-2k)}$
$\nu_c < \nu$	$\frac{p}{2}$	$\frac{k(2+p)-8}{4}$	$\frac{k(2+p)-8}{4(\alpha_s+5-k)}$	$\frac{30p+kp(\alpha_s-8)-8(\alpha_s+5)+2k(\alpha_s+6)}{4(\alpha_s+8-2k)}$	$\frac{8(3p-2-\alpha_s)+kp(\alpha_s-6)+2k(2+\alpha_s)}{4(\alpha_s+6-2k)}$

Table 2. Closure relations of synchrotron afterglow radiation from a quasi-spherical material in a stratified environment

		Coasting Phase			Deceleration Phase			Lateral Expansion	
		Sub-relativistic	Relativistic		Sub-relativistic	Relativistic		Relativistic	
		β	$\alpha(\beta)$		$\alpha(\beta)$	$\alpha(\beta)$		$\alpha(\beta)$	
$\nu_{\text{a},3} < \nu_{\text{c}} < \nu_{\text{m}}$									
$\nu < \nu_{\text{a},3}$	-2	$\frac{(1+k)\beta}{2}$	$\frac{(1+k)\beta}{2}$		$\frac{[5+\alpha_s+k(1+\alpha_s)]\beta}{2(\alpha_s+5-k)}$	$\frac{[8+\alpha_s(1+k)+2(3-k)]\beta}{2(\alpha_s+6-2k)}$			
$\nu_{\text{a},3} < \nu < \nu_{\text{c}}$	$-\frac{1}{3}$	$(11-6k)\beta$	$(11-6k)\beta$		$\frac{[2(5-4k)+\alpha_s(11-6k)]\beta}{\alpha_s+5-k}$	$-\frac{[6k(\alpha_s+1)-4-11\alpha_s]\beta}{\alpha_s+8-2k}$	$-\frac{[18-11\alpha_s+6k(\alpha_s-1)]\beta}{\alpha_s+6-2k}$		
$\nu_{\text{c}} < \nu < \nu_{\text{m}}$	$\frac{1}{2}$	$\frac{(3k-8)\beta}{2}$	$\frac{(3k-8)\beta}{2}$		$-\frac{[2(5-2k)+\alpha_s(8-3k)]\beta}{2(\alpha_s+5-k)}$	$\frac{[8(1-\alpha_s)+k(3\alpha_s-2)]\beta}{2(\alpha_s+8-2k)}$	$\frac{[8(3-k)+\alpha_s(3k-8)]\beta}{2(\alpha_s+6-2k)}$		
$\nu_{\text{m}} < \nu$	$\frac{p}{2}$	$\frac{k(\beta+1)-4}{2}$	$\frac{k(\beta+1)-4}{2}$		$\beta[\frac{30+k(\alpha_s-8)]-4(\alpha_s+5)+k(\alpha_s+6)}{2(\alpha_s+5-k)}$	$\frac{8(6\beta-2-\alpha_s)+2k\beta(\alpha_s-6)+2k(2+\alpha_s)}{4(\alpha_s+8-2k)}$	$\frac{\beta[24+k(\alpha_s-8)]+\alpha_s(k-4)}{2(\alpha_s+6-2k)}$		
$\nu_{\text{a},1} < \nu_{\text{m}} < \nu_{\text{c}}$									
$\nu < \nu_{\text{a},1}$	-2	β	β		$\frac{(\alpha_s+k-1)\beta}{\alpha_s+5-k}$	$\frac{(\alpha_s+2)\beta}{\alpha_s+8-2k}$	$\frac{\alpha_s\beta}{\alpha_s+6-2k}$		
$\nu_{\text{a},1} < \nu < \nu_{\text{m}}$	$-\frac{1}{3}$	$(9-4k)\beta$	$(9-4k)\beta$		$\frac{[3(8+3\alpha_s)-2k(2\alpha_s+5)]\beta}{\alpha_s+5-k}$	$\frac{[6(2-k)+\alpha_s(9-4k)]\beta}{\alpha_s+8-2k}$	$-\frac{[3(2-3\alpha_s)+2k(2\alpha_s-1)]\beta}{\alpha_s+6-2k}$		
$\nu_{\text{m}} < \nu < \nu_{\text{c}}$	$\frac{p-1}{2}$	$\frac{k(\beta+3)-6}{2}$	$\frac{k(\beta+3)-6}{2}$		$\frac{6(5\beta-\alpha_s-1)+k[4+(3\alpha_s+\beta)(\alpha_s-8)]}{2(\alpha_s+5-k)}$	$\frac{\beta[24+\alpha_s k-6k]+3\alpha_s(k-2)+2k}{2(\alpha_s+8-2k)}$	$\frac{\beta[24+k(\alpha_s-8)]+3\alpha_s(k-2)+4(3-k)}{2(\alpha_s+6-2k)}$		
$\nu_{\text{c}} < \nu$	$\frac{p}{2}$	$\frac{k(\beta+1)-4}{2}$	$\frac{k(\beta+1)-4}{2}$		$\frac{\beta[\frac{30+k(\alpha_s-8)]-4(\alpha_s+5)+k(\alpha_s+6)}{2(\alpha_s+5-k)}}$	$\frac{8(6\beta-2-\alpha_s)+2k\beta(\alpha_s-6)+2k(2+\alpha_s)}{4(\alpha_s+8-2k)}$	$\frac{\beta[24+k(\alpha_s-8)]+\alpha_s(k-4)}{2(\alpha_s+6-2k)}$		
$\nu_{\text{m}} < \nu_{\text{a},2} < \nu_{\text{c}}$									
$\nu < \nu_{\text{m}}$	-2	β	β		$\frac{(\alpha_s+k-1)\beta}{\alpha_s+5-k}$	$\frac{(\alpha_s+2)\beta}{\alpha_s+8-2k}$	$\frac{\alpha_s\beta}{\alpha_s+6-2k}$		
$\nu_{\text{m}} < \nu < \nu_{\text{a},2}$	$-\frac{5}{2}$	$\frac{(8+k)\beta}{10}$	$\frac{(8+k)\beta}{10}$		$\frac{[22+\alpha_s(8+k)]\beta}{10(\alpha_s+5-k)}$	$\frac{[8(\alpha_s+5)+k(\alpha_s-6)]\beta}{10(\alpha_s+8-2k)}$	$-\frac{[k(8-\alpha_s)-8(\alpha_s+3)]\beta}{10(\alpha_s+6-2k)}$		
$\nu_{\text{a},2} < \nu < \nu_{\text{c}}$	$\frac{p-1}{2}$	$\frac{k(\beta+3)-6}{2}$	$\frac{k(\beta+3)-6}{2}$		$\frac{6(5\beta-\alpha_s-1)+k[4+(3\alpha_s+\beta)(\alpha_s-8)]}{2(\alpha_s+5-k)}$	$\frac{\beta[24+\alpha_s k-6k]+3\alpha_s(k-2)+2k}{2(\alpha_s+8-2k)}$	$\frac{\beta[24+k(\alpha_s-8)]+3\alpha_s(k-2)+4(3-k)}{2(\alpha_s+6-2k)}$		
$\nu_{\text{c}} < \nu$	$\frac{p}{2}$	$\frac{k(\beta+1)-4}{2}$	$\frac{k(\beta+1)-4}{2}$		$\frac{\beta[\frac{30+k(\alpha_s-8)]-4(\alpha_s+5)+k(\alpha_s+6)}{2(\alpha_s+5-k)}}$	$\frac{8(6\beta-2-\alpha_s)+2k\beta(\alpha_s-6)+2k(2+\alpha_s)}{4(\alpha_s+8-2k)}$	$\frac{\beta[24+k(\alpha_s-8)]+\alpha_s(k-4)}{2(\alpha_s+6-2k)}$		

Table 3. Evolution of the density parameter $F_\nu \propto A_k^{\alpha_k}$ in each cooling condition of the synchrotron afterglow model

	Coasting Phase			Deceleration Phase		Lateral Expansion
	Sub-relativistic		Relativistic	Sub-relativistic		Relativistic
	β	$\alpha(\beta)$		$\alpha(\beta)$	$\alpha(\beta)$	$\alpha(\beta)$
	β	α_k		α_k		
$\nu_{a,3} < \nu_c < \nu_m$						
$\nu < \nu_{a,3}$	-2	-1	-1	$-\frac{5+\alpha_s}{\alpha_s+5-k}$	$-\frac{\alpha_s+8}{\alpha_s+8-2k}$	$-\frac{6+\alpha_s}{\alpha_s+6-2k}$
$\nu_{a,3} < \nu < \nu_c$	$-\frac{1}{3}$	2	2	$\frac{5+2\alpha_s}{\alpha_s+5-k}$	$\frac{2(10+3\alpha_s)}{3(\alpha_s+8-2k)}$	$\frac{2(4+3\alpha_s)}{3(\alpha_s+6-2k)}$
$\nu_c < \nu < \nu_m$	$\frac{1}{2}$	$\frac{3}{4}$	$\frac{3}{4}$	$\frac{5+3\alpha_s}{4(\alpha_s+5-k)}$	$\frac{3\alpha_s}{4(\alpha_s+8-2k)}$	$\frac{3(\alpha_s-2)}{4(\alpha_s+6-2k)}$
$\nu_m < \nu$	$\frac{p}{2}$	$\frac{p+2}{4}$	$\frac{p+2}{4}$	$\frac{2(5+\alpha_s)+p(\alpha_s-5)}{4(\alpha_s+5-k)}$	$\frac{(p+2)\alpha_s}{4(\alpha_s+8-2k)}$	$\frac{(p+2)(\alpha_s-2)}{4(\alpha_s+6-2k)}$
$\nu_{a,1} < \nu_m < \nu_c$						
$\nu < \nu_{a,1}$	-2	0	0	$-\frac{4}{\alpha_s+5-k}$	$-\frac{4}{\alpha_s+8-2k}$	$-\frac{4}{\alpha_s+6-2k}$
$\nu_{a,1} < \nu < \nu_m$	$-\frac{1}{3}$	$\frac{4}{3}$	$\frac{4}{3}$	$\frac{13+4\alpha_s}{3(\alpha_s+5-k)}$	$\frac{4(\alpha_s+3)}{3(\alpha_s+8-2k)}$	$\frac{4(\alpha_s+1)}{3(\alpha_s+6-2k)}$
$\nu_m < \nu < \nu_c$	$\frac{p-1}{2}$	$\frac{p+5}{4}$	$\frac{p+5}{4}$	$\frac{19+5\alpha_s+p(\alpha_s-5)}{4(\alpha_s+5-k)}$	$\frac{16+(p+5)\alpha_s}{4(\alpha_s+8-2k)}$	$\frac{6+5\alpha_s+p(\alpha_s-2)}{4(\alpha_s+6-2k)}$
$\nu_c < \nu$	$\frac{p}{2}$	$\frac{p+2}{4}$	$\frac{p+2}{4}$	$\frac{2(5+\alpha_s)+p(\alpha_s-5)}{4(\alpha_s+5-k)}$	$\frac{(p+2)\alpha_s}{4(\alpha_s+8-2k)}$	$\frac{(p+2)(\alpha_s-2)}{4(\alpha_s+6-2k)}$
$\nu_m < \nu_{a,2} < \nu_c$						
$\nu < \nu_m$	-2	0	0	$-\frac{4}{\alpha_s+5-k}$	$-\frac{4}{\alpha_s+8-2k}$	$-\frac{4}{\alpha_s+6-2k}$
$\nu_m < \nu < \nu_{a,2}$	$-\frac{5}{2}$	$-\frac{1}{4}$	$-\frac{1}{4}$	$-\frac{11+\alpha_s}{4(\alpha_s+5-k)}$	$-\frac{16+\alpha_s}{4(\alpha_s+8-2k)}$	$-\frac{14+\alpha_s}{4(\alpha_s+6-2k)}$
$\nu_{a,2} < \nu < \nu_c$	$\frac{p-1}{2}$	$\frac{p+5}{4}$	$\frac{p+5}{4}$	$\frac{19+5\alpha_s+p(\alpha_s-5)}{4(\alpha_s+5-k)}$	$\frac{16+(p+5)\alpha_s}{4(\alpha_s+8-2k)}$	$\frac{6+5\alpha_s+p(\alpha_s-2)}{4(\alpha_s+6-2k)}$
$\nu_c < \nu$	$\frac{p}{2}$	$\frac{p+2}{4}$	$\frac{p+2}{4}$	$\frac{2(5+\alpha_s)+p(\alpha_s-5)}{4(\alpha_s+5-k)}$	$\frac{(p+2)\alpha_s}{4(\alpha_s+8-2k)}$	$\frac{(p+2)(\alpha_s-2)}{4(\alpha_s+6-2k)}$

Table 4. The best-fit values found with MCMC simulations after describing the multiwavelength afterglow observations with a synchrotron model evolving in a constant medium.

GRB Name	$\log_{10}(E/\text{erg})$	$\log_{10}(n/\text{cm}^{-3})$	Γ_0	$\log_{10}(\varepsilon_e)$	$\log_{10}(\varepsilon_B)$	p	α	θ_c
980425	$51.993^{+0.009}_{-0.010}$	$-0.119^{+0.009}_{-0.008}$	$3.758^{+0.012}_{-0.011}$	$-1.023^{+0.011}_{-0.010}$	$-1.478^{+0.010}_{-0.011}$	$2.803^{+0.009}_{-0.010}$	$2.000^{+0.011}_{-0.009}$	$50.305^{+0.011}_{-0.011}$
031203	$52.000^{+0.010}_{-0.010}$	$0.254^{+0.009}_{-0.010}$	$2.870^{+0.012}_{-0.009}$	$-0.110^{+0.010}_{-0.010}$	$-1.001^{+0.010}_{-0.010}$	$2.059^{+0.010}_{-0.011}$	$3.001^{+0.008}_{-0.011}$	$32.019^{+0.011}_{-0.009}$
060218	$49.751^{+0.010}_{-0.010}$	$0.473^{+0.010}_{-0.010}$	$2.111^{+0.011}_{-0.009}$	$-0.264^{+0.010}_{-0.010}$	$-4.772^{+0.010}_{-0.010}$	$3.030^{+0.009}_{-0.010}$	$2.999^{+0.009}_{-0.010}$	$46.009^{+0.010}_{-0.010}$
100316D	$51.994^{+0.010}_{-0.010}$	$0.756^{+0.010}_{-0.009}$	$1.703^{+0.010}_{-0.010}$	$-2.034^{+0.010}_{-0.011}$	$-1.663^{+0.009}_{-0.011}$	$2.500^{+0.009}_{-0.010}$	$2.999^{+0.011}_{-0.010}$	$51.932^{+0.009}_{-0.010}$
130603B	$51.474^{+0.009}_{-0.011}$	$0.010^{+0.010}_{-0.010}$	$4.799^{+0.012}_{-0.009}$	$-0.797^{+0.010}_{-0.010}$	$-1.981^{+0.010}_{-0.010}$	$2.027^{+0.010}_{-0.010}$	$2.301^{+0.009}_{-0.011}$	$44.963^{+0.010}_{-0.010}$
150101B	$51.992^{+0.011}_{-0.010}$	$-0.001^{+0.010}_{-0.009}$	$4.480^{+0.010}_{-0.010}$	$-0.393^{+0.011}_{-0.010}$	$-1.934^{+0.011}_{-0.009}$	$2.533^{+0.010}_{-0.009}$	$2.163^{+0.010}_{-0.011}$	$43.981^{+0.010}_{-0.010}$
171205A	$52.000^{+0.002}_{-0.002}$	$1.000^{+0.002}_{-0.002}$	$4.894^{+0.002}_{-0.002}$	$-0.097^{+0.002}_{-0.002}$	$-2.000^{+0.002}_{-0.002}$	$2.266^{+0.002}_{-0.002}$	$2.000^{+0.002}_{-0.002}$	$54.844^{+0.002}_{-0.002}$

Table 5. The best-fit values found with MCMC simulations after describing the multiwavelength afterglow observations with a synchrotron model evolving in a wind-like medium.

GRB Name	$\log_{10}(E/\text{erg})$	$\log_{10}(n/\text{cm}^{-3})$	Γ_0	$\log_{10}(\varepsilon_e)$	$\log_{10}(\varepsilon_B)$	p	α_s	θ_c
980425	$45.035^{+0.058}_{-0.026}$	$-1.737^{+0.416}_{-0.196}$	$5.506^{+3.071}_{-3.064}$	$-0.261^{+0.054}_{-0.053}$	$-0.417^{+0.089}_{-0.173}$	$2.434^{+0.004}_{-0.003}$	$2.004^{+0.006}_{-0.003}$	$42.529^{+8.482}_{-8.505}$
031203	$47.600^{+0.110}_{-0.108}$	$0.827^{+0.099}_{-0.090}$	$5.477^{+0.112}_{-0.093}$	$-0.519^{+0.090}_{-0.089}$	$-0.543^{+0.109}_{-0.091}$	$2.484^{+0.106}_{-0.091}$	$2.013^{+0.089}_{-0.100}$	$42.473^{+0.109}_{-0.096}$
060218	$50.035^{+0.288}_{-0.256}$	$0.789^{+0.157}_{-0.344}$	$5.533^{+3.047}_{-3.057}$	$-0.518^{+0.013}_{-0.029}$	$-0.557^{+0.043}_{-0.094}$	$2.670^{+0.011}_{-0.008}$	$2.022^{+0.037}_{-0.017}$	$42.547^{+8.508}_{-8.484}$
100316D	$50.845^{+0.517}_{-0.507}$	$0.607^{+0.293}_{-0.615}$	$5.534^{+3.029}_{-3.090}$	$-0.533^{+0.024}_{-0.052}$	$-0.605^{+0.078}_{-0.172}$	$2.667^{+0.019}_{-0.015}$	$2.047^{+0.078}_{-0.035}$	$42.675^{+8.440}_{-8.608}$
171205A	$51.895^{+0.078}_{-0.165}$	$-1.668^{+1.858}_{-2.164}$	$5.494^{+3.066}_{-3.052}$	$-1.417^{+0.241}_{-0.208}$	$-3.677^{+0.470}_{-0.239}$	$2.845^{+0.008}_{-0.008}$	$2.887^{+0.052}_{-0.050}$	$42.527^{+8.475}_{-8.535}$

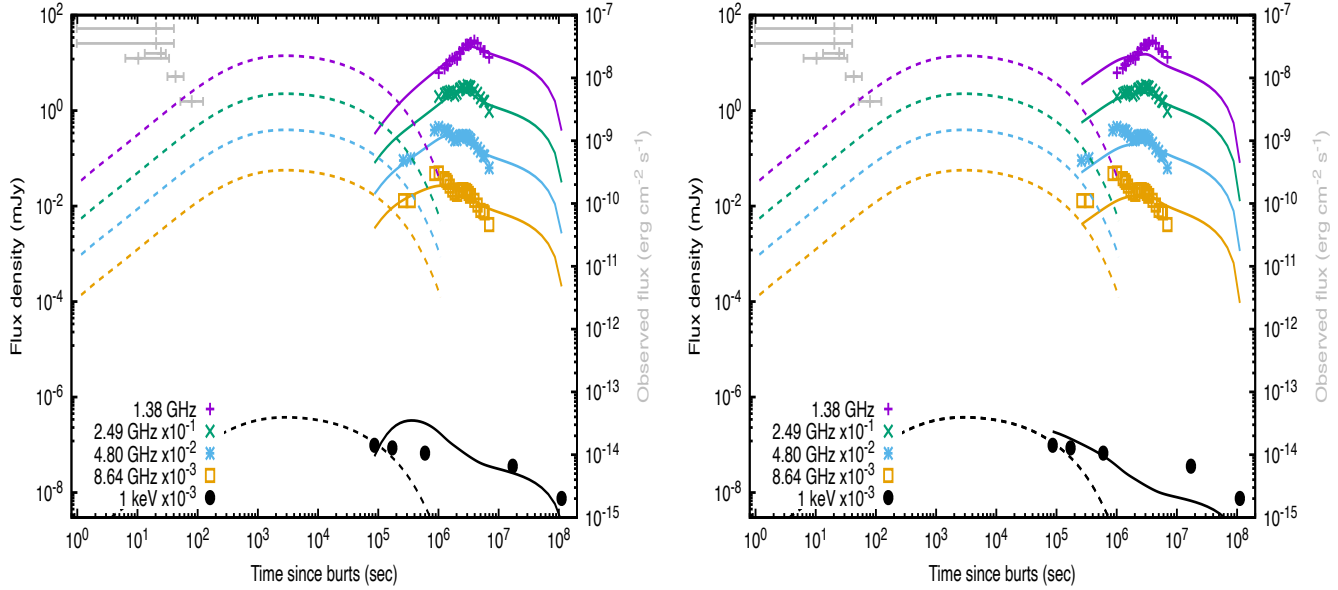


Figure 1. Multiwavelength observations of GRB 980425 with the best-fit curves obtained with the synchrotron afterglow model of quasi-spherical outflow (solid line) evolving in a constant (left) and wind-like (right) medium. The dashed line corresponds to a narrow jet introduced to describe the early X-ray observations. Details of the narrow jet can be found in (Fraija et al. 2019c). Radio data taken from Kulkarni et al. (1998), X-Ray data taken from Pian et al. (2000, 2004); Kouveliotou et al. (2004).

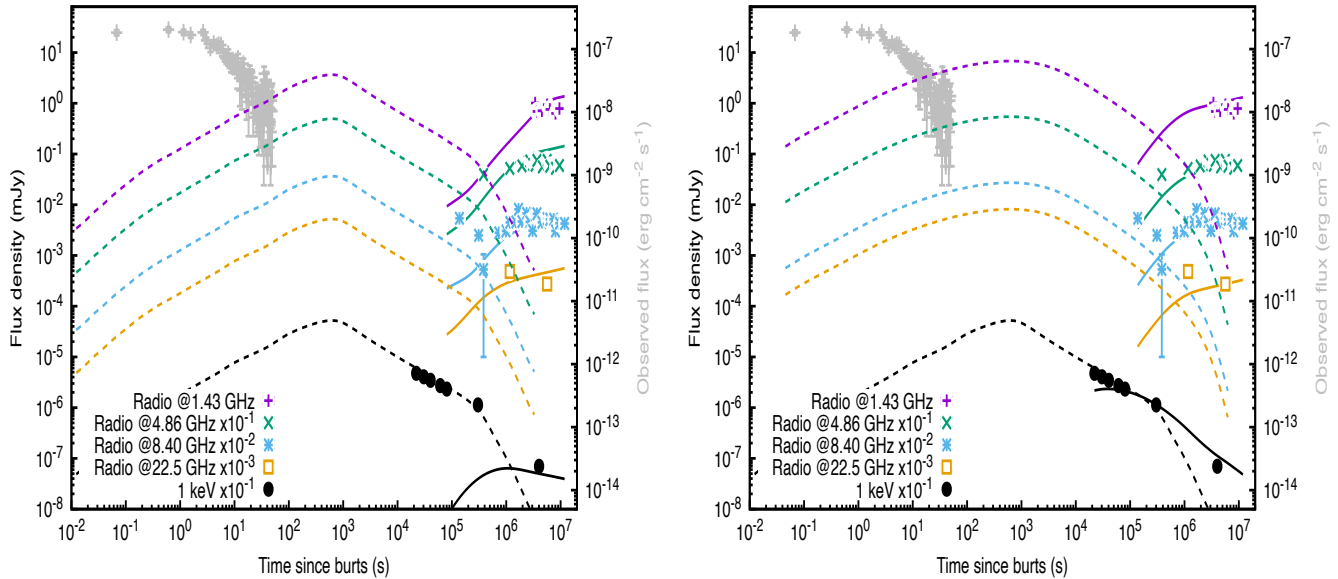


Figure 2. Same as Figure 1, but for GRB 031203. Radio data taken from Soderberg et al. (2004), X-Ray data taken from Watson et al. (2004).

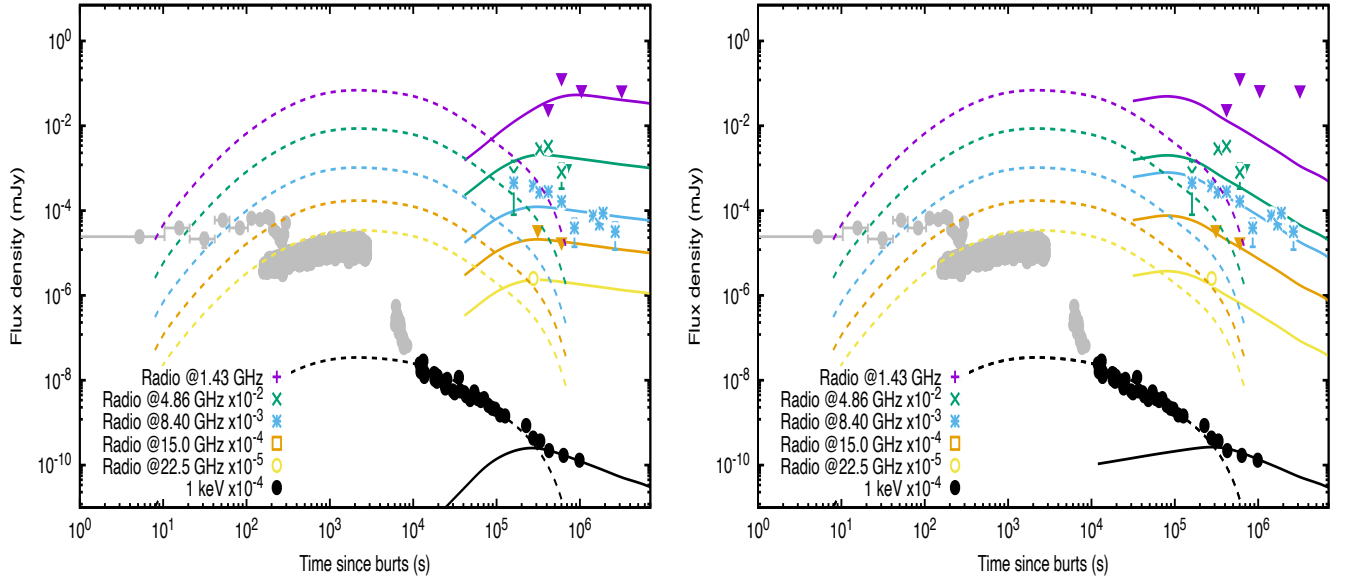


Figure 3. Same as Figure 1, but for GRB 060218. Radio data taken from Soderberg et al. (2006a), X-Ray data taken from Campana & et al. (2006).

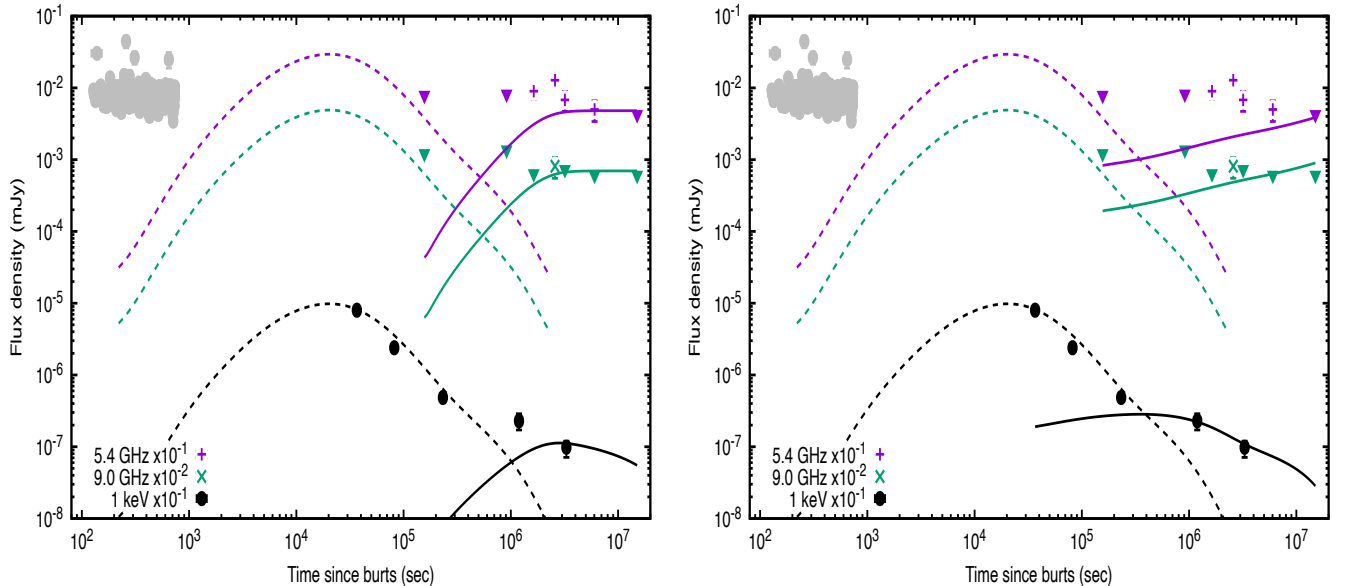


Figure 4. Same as Figure 1, but for GRB 100316D. Data taken from Margutti et al. (2013).

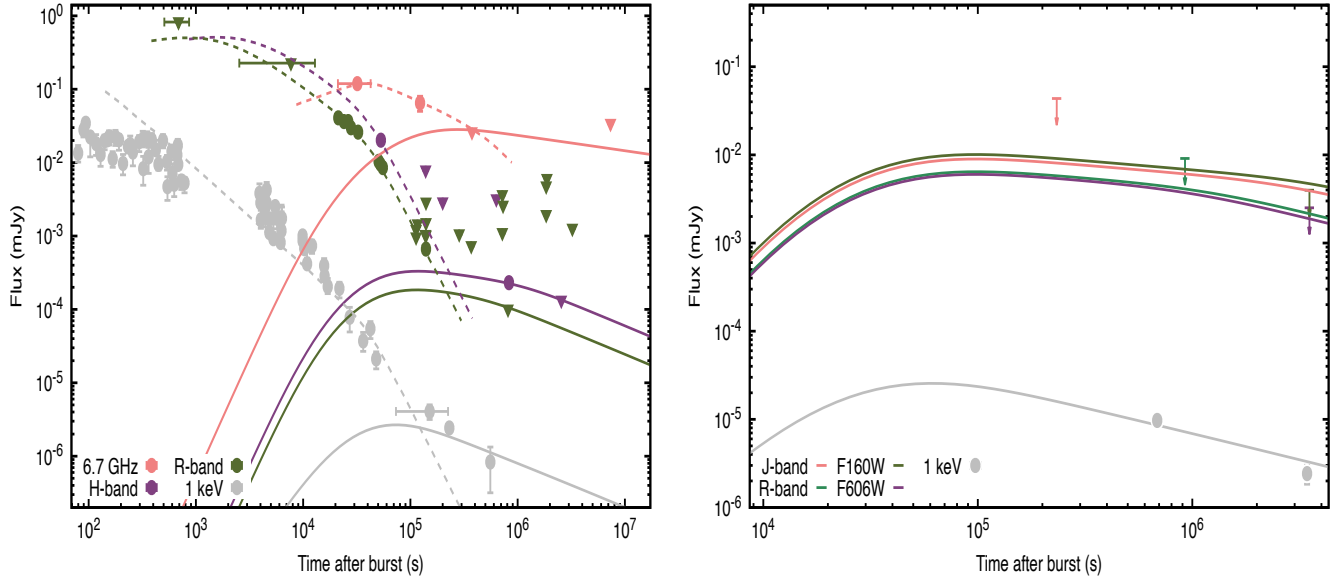


Figure 5. Same as Figure 1, but for GRB 130603B and GRB 150101B. For GRB 130603B the radio data was taken from Fong et al. (2014); Berger et al. (2013); Tanvir et al. (2013), optical data was taken from Cucchiara et al. (2013); Tanvir et al. (2013); Fong et al. (2014); de Ugarte Postigo et al. (2014) and X-Ray data from Fong et al. (2014). Meanwhile, for GRB 150101B data was taken from Fong et al. (2016).

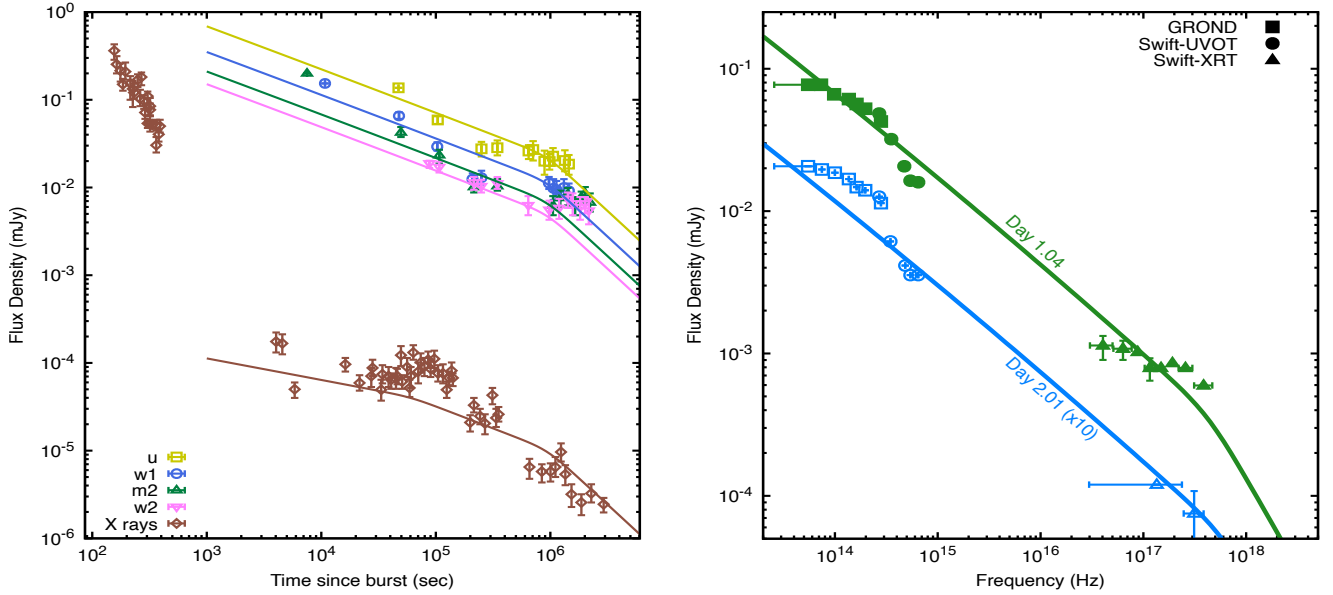


Figure 6. Multiwavelength light curves (left) and SED (right) observations of GRB 171205A with the best-fit curves obtained with the synchrotron afterglow model evolving in a wind-like medium. Data taken from Izzo et al. (2019).

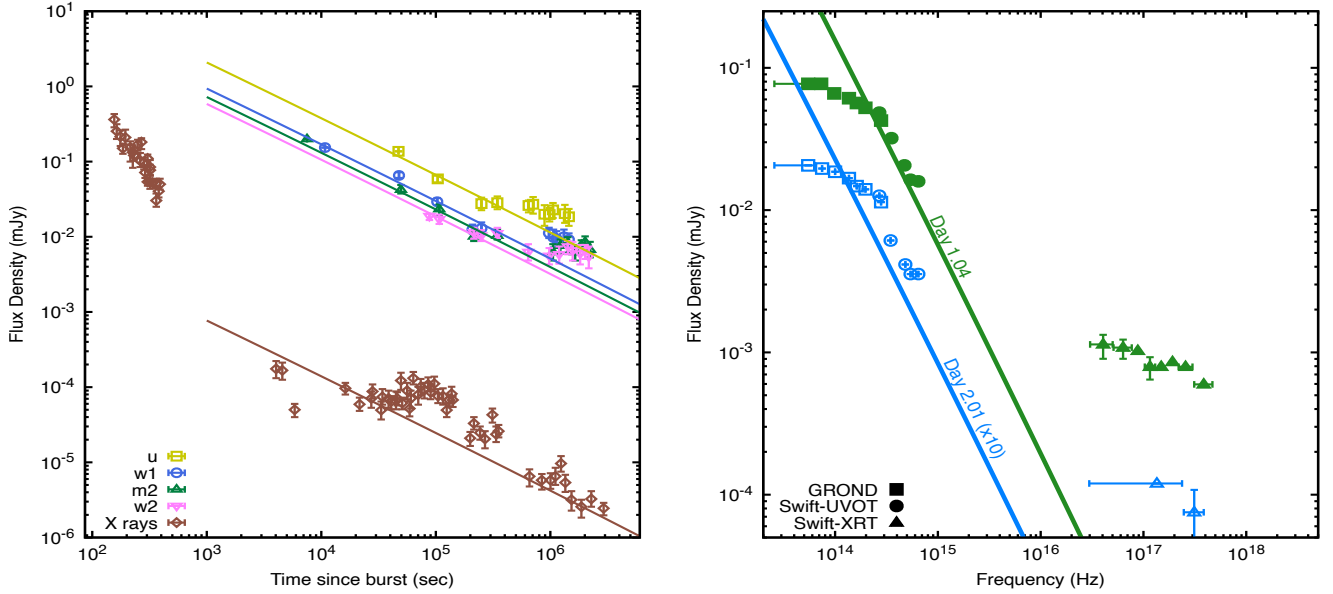


Figure 7. Multiwavelength light curves (left) and SED (right) observations of GRB 171205A with the best-fit curves obtained with the synchrotron afterglow model for a constant circuburst like medium. Data taken from [Izzo et al. \(2019\)](#).

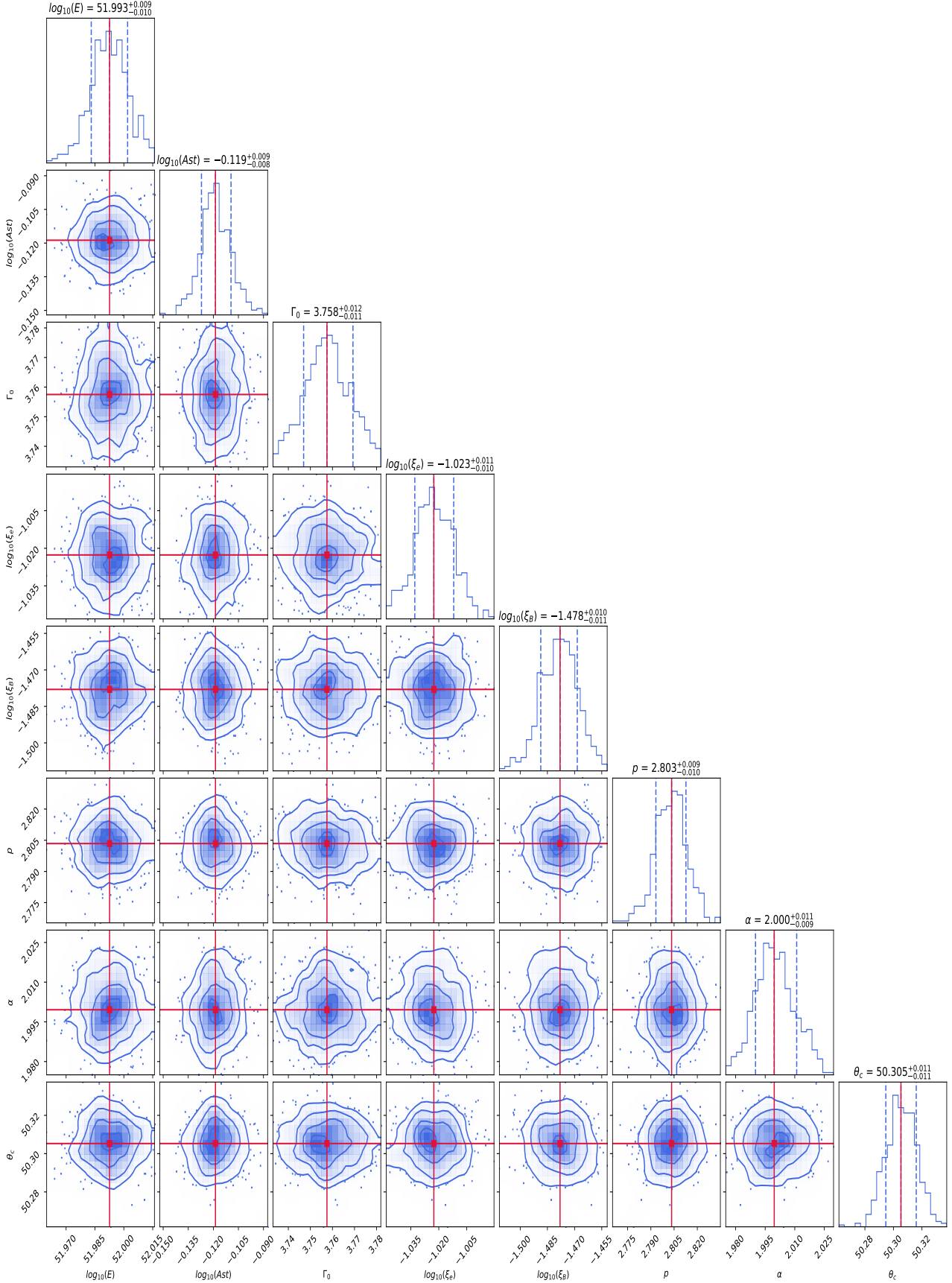


Figure 8. Corner plot of the parameters obtained from describing the multiwavelength observations of GRB 980425. Red lines show the best-fit values which are reported in Table 4.

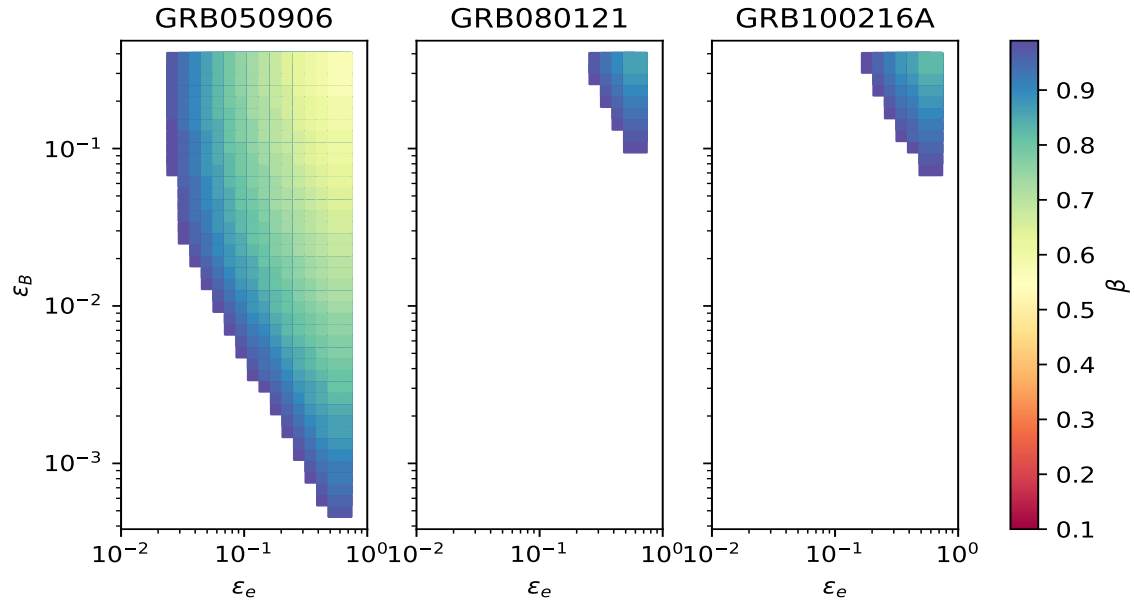


Figure 9. The 3D parameter space of the rejected values of ε_B as a function of β and ε_e for $n = 1 \text{ cm}^{-3}$, $E = 10^{50} \text{ erg}$, $\alpha_s = 2$ and $p = 2.2$.

APPENDIX A: SYNCHROTRON FORWARD-SHOCK SCENARIO FROM A COCOON MATERIAL

A1 Mildly-relativistic regime

Hereafter, we report the proportionality constants with the values of $k = 2$ for $n = A_{\text{st}} 3 \times 10^{35} \text{ cm}^{-1} r^{-2}$, $p = 2.4$ and $\alpha_s = 2$.

A1.0.1 Coasting phase A constant bulk Lorentz factor characterizes the coasting phase. For the lowest energy electrons and for those with energy above which they cool effectively, the Lorentz factors are

$$\begin{aligned}\gamma_m &= 1.65 \times 10^2 g(p) \varepsilon_{e,-1} \zeta_e^{-1} \Gamma_{0,0.5}, \\ \gamma_c &= 8.79 \left(\frac{1+z}{1.05} \right)^{1-k} (1+Y)^{-1} \varepsilon_{B,-3}^{-1} A_{\text{st}}^{-1} \Gamma_{0,0.5}^{2k-3} t_3^{k-1}.\end{aligned}\quad (\text{A1})$$

The characteristic and cooling synchrotron breaks and the maximum synchrotron flux become

$$\begin{aligned}\nu_m &\simeq 8.57 \times 10^{12} \text{ Hz} \left(\frac{1+z}{1.05} \right)^{\frac{k-2}{2}} \zeta_e^{-2} g^2(p) \varepsilon_{e,-1}^2 \varepsilon_{B,-3}^{\frac{1}{2}} A_{\text{st}}^{\frac{1}{2}} \Gamma_{0,0.5}^{4-k} t_3^{-\frac{k}{2}}, \\ \nu_c &\simeq 3.55 \times 10^{11} \text{ Hz} \left(\frac{1+z}{1.05} \right)^{\frac{2-3k}{2}} (1+Y)^{-2} \varepsilon_{B,-3}^{-\frac{3}{2}} A_{\text{st}}^{-\frac{3}{2}} \Gamma_{0,0.5}^{3k-4} t_3^{\frac{3k-4}{2}}, \\ F_{\text{max}} &\simeq 4.80 \text{ mJy} \left(\frac{1+z}{1.05} \right)^{\frac{3k-2}{2}} \zeta_e \varepsilon_{B,-3}^{\frac{1}{2}} d_{z,26.78}^{-2} A_{\text{st}}^{\frac{3}{2}} \Gamma_{0,0.5}^{8-3k} t_3^{\frac{3(2-k)}{2}}.\end{aligned}\quad (\text{A2})$$

The synchrotron spectral breaks in the self-absorption regime can be expressed as

$$\begin{aligned}\nu_{a,1} &\simeq 3.45 \times 10^4 \text{ Hz} \left(\frac{1+z}{1.05} \right)^{\frac{4(k-2)}{5}} \zeta_e g(p)^{-1} \varepsilon_{e,-1}^{-1} \varepsilon_{B,-3}^{\frac{1}{5}} A_{\text{st}}^{\frac{4}{5}} \Gamma_{0,0.5}^{\frac{8(1-k)}{5}} t_3^{\frac{3-4k}{5}}, \\ \nu_{a,2} &\simeq 3.63 \times 10^8 \text{ Hz} \left(\frac{1+z}{1.05} \right)^{\frac{(k-2)(p+6)}{2(p+4)}} \zeta_e^{-\frac{2(p-1)}{p+4}} g(p)^{\frac{2(p-1)}{p+4}} \varepsilon_{B,-3}^{\frac{p+2}{p+4}} \varepsilon_{e,-1}^{\frac{2(p-1)}{p+4}} A_{\text{st}}^{\frac{p+6}{2(p+4)}} \Gamma_{0,0.5}^{\frac{4(p+2)-k(p+6)}{p+4}} t_3^{\frac{4-k(p+6)}{2(p+4)}}, \\ \nu_{a,3} &\simeq 9.48 \times 10^6 \text{ Hz} \left(\frac{1+z}{1.05} \right)^{\frac{13-9k}{5}} (1+Y) \varepsilon_{B,-3}^{\frac{6}{5}} A_{\text{st}}^{\frac{9}{5}} \Gamma_{0,0.5}^{\frac{2(14-9k)}{5}} t_3^{\frac{8-9k}{5}}.\end{aligned}\quad (\text{A3})$$

Table 1 shows the evolution of synchrotron light curves across the spectral and temporal indices, given the spectral breaks and maximum flux from eqs. A2 and A3. Also presented in Table 2 are the closure relations for each cooling condition seen during the coasting phase.

A1.0.2 Deceleration phase During the deceleration phase, the Lorentz factor of the lowest energy electrons and the one of those with energy above which they cool effectively are

$$\begin{aligned}\gamma_m &= 1.41 \times 10^2 \left(\frac{1+z}{1.05} \right)^{-\frac{k-3}{\alpha_s+8-2k}} \zeta_e^{-1} g(p) \varepsilon_{e,-1} A_{\text{st}}^{-\frac{1}{\alpha_s+8-2k}} \tilde{E}_{50}^{\frac{1}{\alpha_s+8-2k}} t_4^{\frac{k-3}{\alpha_s+8-2k}}, \\ \gamma_c &= 7.48 \times 10^1 \left(\frac{1+z}{1.05} \right)^{-\frac{k+1+\alpha_s(k-1)}{\alpha_s+8-2k}} (1+Y)^{-1} \varepsilon_{B,-3}^{-1} A_{\text{st}}^{-\frac{\alpha_s+5}{\alpha_s+8-2k}} \tilde{E}_{50}^{\frac{2k-3}{\alpha_s+8-2k}} t_4^{\frac{1-\alpha_s+k(\alpha_s+1)}{\alpha_s+8-2k}}.\end{aligned}\quad (\text{A4})$$

The characteristic and cooling synchrotron breaks and the maximum synchrotron flux become

$$\begin{aligned}\nu_m &\simeq 6.21 \times 10^{11} \text{ Hz} \left(\frac{1+z}{1.05} \right)^{\frac{8+\alpha_s(k-2)-2k}{2(\alpha_s+8-2k)}} \zeta_e^{-2} g^2(p) \varepsilon_{e,-1}^2 \varepsilon_{B,-3}^{\frac{1}{2}} A_{\text{st}}^{\frac{\alpha_s}{16+2\alpha_s-4k}} \tilde{E}_{50}^{\frac{4-k}{\alpha_s+8-2k}} t_4^{-\frac{24+(\alpha_s-6)k}{2(\alpha_s+8-2k)}}, \\ \nu_c &\simeq 4.46 \times 10^{12} \text{ Hz} \left(\frac{1+z}{1.05} \right)^{-\frac{8-2\alpha_s+k+3\alpha_s k}{2(\alpha_s+8-2k)}} \varepsilon_{B,-3}^{-\frac{3}{2}} (1+Y)^{-2} A_{\text{st}}^{-\frac{16+3\alpha_s}{2(\alpha_s+8-2k)}} \tilde{E}_{50}^{\frac{3k-4}{\alpha_s+8-2k}} t_4^{\frac{(\alpha_s+2)(3k-4)}{2(\alpha_s+8-2k)}}, \\ F_{\text{max}} &\simeq 3.48 \text{ mJy} \left(\frac{1+z}{1.05} \right)^{\frac{32+3k(\alpha_s-2)-2\alpha_s}{2(\alpha_s+8-2k)}} \zeta_e \varepsilon_{B,-3}^{\frac{1}{2}} d_{z,26.78}^{-2} A_{\text{st}}^{\frac{3\alpha_s+8}{2(\alpha_s+8-2k)}} \tilde{E}_{50}^{\frac{8-3k}{\alpha_s+8-2k}} t_4^{-\frac{3\alpha_s(k-2)+2k}{2(\alpha_s+8-2k)}}.\end{aligned}\quad (\text{A5})$$

The synchrotron spectral breaks in the self-absorption regime can be expressed as

$$\begin{aligned}\nu_{a,1} &\simeq 4.46 \times 10^3 \text{ Hz} \left(\frac{1+z}{1.05} \right)^{\frac{4k(\alpha_s+4)-8(\alpha_s+5)}{5(\alpha_s+8-2k)}} \zeta_e g(p)^{-1} \varepsilon_{e,-1}^{-1} \varepsilon_{B,-3}^{\frac{1}{5}} A_k^{\frac{4(\alpha_s+6)}{5(\alpha_s+8-2k)}} \tilde{E}_{50}^{\frac{8(1-k)}{5(\alpha_s+8-2k)}} t_4^{\frac{3\alpha_s-2k(2\alpha_s+3)}{5(\alpha_s+8-2k)}}, \\ \nu_{a,2} &\simeq 3.56 \times 10^7 \text{ Hz} \left(\frac{1+z}{1.05} \right)^{\frac{k[20+p(\alpha_s-2)+6\alpha_s]-2[p(\alpha_s-4)+6(\alpha_s+4)]}{2(p+4)(\alpha_s+8-2k)}} \zeta_e^{-\frac{2(p-1)}{p+4}} g(p)^{\frac{2(p-1)}{p+4}} \varepsilon_{B,-3}^{\frac{p+2}{2(p+4)}} \varepsilon_{e,-1}^{\frac{2(p-1)}{p+4}} A_{\text{st}}^{\frac{32+\alpha_s(p+6)}{2(p+4)(\alpha_s+8-2k)}} \\ &\quad \times \tilde{E}_{50}^{\frac{4(p+2)-k(p+6)}{(p+4)(\alpha_s+8-2k)}} t_4^{-\frac{4(4+6p-\alpha_s)+k[4+6\alpha_s+p(\alpha_s-6)]}{2(p+4)(\alpha_s+8-2k)}}, \\ \nu_{a,3} &\simeq 2.13 \times 10^5 \text{ Hz} \left(\frac{1+z}{1.05} \right)^{-\frac{20+13\alpha_s-k(9\alpha_s+16)}{5(\alpha_s+8-2k)}} (1+Y) \varepsilon_{B,-3}^{\frac{6}{5}} A_{\text{st}}^{\frac{44+9\alpha_s}{5(\alpha_s+8-2k)}} \tilde{E}_{50}^{\frac{2(14-9k)}{5(\alpha_s+8-2k)}} t_4^{-\frac{20-8\alpha_s+3k(2+3\alpha_s)}{5(\alpha_s+8-2k)}}.\end{aligned}\quad (\text{A6})$$

Table 1 shows the evolution of synchrotron light curves across the spectral and temporal indices, given the spectral breaks and maximum flux from eqs. A5 and A6. Also presented in Table 2 are the closure relations for each cooling condition seen during the deceleration phase.

A1.0.3 Post-jet-break decay phase During the post-jet-break decay phase, the Lorentz factor of the lowest energy electrons and the one of those with energy above which they cool effectively are

$$\begin{aligned}\gamma_m &= 6.53 \times 10^1 \left(\frac{1+z}{1.05} \right)^{\frac{3-k}{\alpha_s+6-2k}} \zeta_e^{-1} g(p) \beta^{-\frac{\alpha_s}{\alpha_s+6-2k}} \varepsilon_{e,-1} A_{st}^{-\frac{1}{\alpha_s+6-2k}} \tilde{E}_{50}^{\frac{1}{\alpha_s+6-2k}} t_6^{\frac{k-3}{\alpha_s+6-2k}}, \\ \gamma_c &= 3.47 \times 10^3 \left(\frac{1+z}{1.05} \right)^{\frac{\alpha_s+k-3-\alpha_s k}{\alpha_s+6-2k}} \beta^{\frac{\alpha_s(3-2k)}{\alpha_s+6-2k}} (1+Y)^{-1} \varepsilon_{B,-3}^{-1} A_{st}^{-\frac{\alpha_s+3}{\alpha_s+6-2k}} \tilde{E}_{50}^{\frac{2k-3}{\alpha_s+6-2k}} t_6^{\frac{3-\alpha_s+k(\alpha_s-1)}{\alpha_s+6-2k}}.\end{aligned}\quad (A7)$$

The characteristic and cooling synchrotron breaks and the maximum synchrotron flux become

$$\begin{aligned}\nu_m &\simeq 1.33 \times 10^9 \text{ Hz} \left(\frac{1+z}{1.05} \right)^{\frac{12-2\alpha_s-4k+\alpha_s k}{2(\alpha_s+6-2k)}} \zeta_e^{-2} g^2(p) \beta^{\frac{\alpha_s(k-4)}{\alpha_s+6-2k}} \varepsilon_{e,-1}^2 \varepsilon_{B,-3}^{\frac{1}{2}} A_{st}^{\frac{\alpha_s-2}{2(\alpha_s+6-2k)}} \tilde{E}_{50}^{\frac{4-k}{\alpha_s+6-2k}} t_6^{-\frac{24+(\alpha_s-8)k}{2(\alpha_s+6-2k)}}, \\ \nu_c &\simeq 8.57 \times 10^{14} \text{ Hz} \left(\frac{1+z}{1.05} \right)^{\frac{\alpha_s(2-3k)+4(k-3)}{2(\alpha_s+6-2k)}} (1+Y)^{-2} \beta^{\frac{\alpha_s(4-3k)}{\alpha_s+6-2k}} \varepsilon_{B,-3}^{-\frac{3}{2}} A_{st}^{-\frac{10+3\alpha_s}{2(\alpha_s+6-2k)}} \tilde{E}_{50}^{\frac{3k-4}{\alpha_s+6-2k}} t_6^{\frac{\alpha_s(3k-4)}{2(\alpha_s+6-2k)}}, \\ F_{\max} &\simeq 7.49 \times 10^{-1} \text{ mJy} \left(\frac{1+z}{1.05} \right)^{\frac{36-2\alpha_s+3k(\alpha_s-4)}{2(\alpha_s+6-2k)}} \zeta_e \beta^{\frac{\alpha_s(3k-8)}{\alpha_s+6-2k}} \varepsilon_{B,-3}^{\frac{1}{2}} d_{z,26.78}^{-2} A_{st}^{\frac{3\alpha_s+2}{2(\alpha_s+6-2k)}} \tilde{E}_{50}^{\frac{8-3k}{\alpha_s+6-2k}} t_6^{\frac{4(k-3)-3\alpha_s(k-2)}{2(\alpha_s+6-2k)}}.\end{aligned}\quad (A8)$$

The synchrotron spectral breaks in the self-absorption regime can be expressed as

$$\begin{aligned}\nu_{a,1} &\simeq 1.52 \times 10^2 \text{ Hz} \left(\frac{1+z}{1.05} \right)^{\frac{4k(\alpha_s+2)-8(\alpha_s+3)}{3(\alpha_s+6-2k)}} \zeta_e g(p)^{-1} \beta^{\frac{8\alpha_s(k-1)}{5(\alpha_s+6-2k)}} \varepsilon_{e,-1}^{-1} \varepsilon_{B,-3}^{\frac{1}{5}} A_{st}^{\frac{4(\alpha_s+4)}{5(\alpha_s+6-2k)}} \tilde{E}_{50}^{\frac{8(1-k)}{5(\alpha_s+6-2k)}} t_6^{\frac{3(\alpha_s-2)+2k(1-2\alpha_s)}{5(\alpha_s+6-2k)}}, \\ \nu_{a,2} &\simeq 3.24 \times 10^5 \text{ Hz} \left(\frac{1+z}{1.05} \right)^{\frac{k[8+p(\alpha_s-4)+6\alpha_s]-2[p(\alpha_s-6)+6(\alpha_s+2)]}{2(p+4)(\alpha_s+6-2k)}} \zeta_e^{-\frac{2(p-1)}{p+4}} g(p)^{\frac{2(p-1)}{p+4}} \beta^{\frac{\alpha_s[k(p+6)-4(p+2)]}{(p+4)(\alpha_s+6-2k)}} \varepsilon_{B,-3}^{\frac{p+2}{2(p+4)}} \varepsilon_{e,-1}^{\frac{2(p-1)}{p+4}} A_{st}^{\frac{20+p(\alpha_s-2)+6\alpha_s}{2(p+4)(\alpha_s+6-2k)}} \\ &\quad \times \tilde{E}_{50}^{\frac{4(p+2)-k(p+6)}{(p+4)(\alpha_s+6-2k)}} t_6^{-\frac{4(6+6p-\alpha_s)+k[-8+p(\alpha_s-8)+6\alpha_s]}{2(p+4)(\alpha_s+6-2k)}}, \\ \nu_{a,3} &\simeq 1.61 \times 10^2 \text{ Hz} \left(\frac{1+z}{1.05} \right)^{\frac{6-13\alpha_s+k(9\alpha_s-2)}{5(\alpha_s+6-2k)}} (1+Y) \beta^{\frac{2\alpha_s(9k-14)}{5(\alpha_s+6-2k)}} \varepsilon_{B,-3}^{\frac{6}{5}} A_{st}^{\frac{26+9\alpha_s}{5(\alpha_s+6-2k)}} \tilde{E}_{50}^{\frac{2(14-9k)}{5(\alpha_s+6-2k)}} t_6^{-\frac{2[36-8\alpha_s+3k(3\alpha_s-4)]}{5(\alpha_s+6-2k)}}.\end{aligned}\quad (A9)$$

Table 1 shows the evolution of synchrotron light curves across the spectral and temporal indices, given the spectral breaks and maximum flux from eqs. A8 and A9. Also presented in Table 2 are the closure relations for each cooling condition seen during the post-jet-break decay phase.

A2 Sub-relativistic regime

A2.0.1 Coasting phase A constant velocity characterizes the coasting phase. For the lowest energy electrons and for those with energy above which they cool effectively, the Lorentz factors are

$$\begin{aligned}\gamma_m &= 7.55 \times 10^1 g(p) \varepsilon_{e,-1} \zeta_e^{-1} \beta_{-0.22}^2, \\ \gamma_c &= 2.15 \times 10^2 \left(\frac{1+z}{1.05} \right)^{1-k} (1+Y)^{-1} \varepsilon_{B,-3}^{-1} A_{st}^{-1} \beta_{-0.22}^{k-2} t_5^{k-1}.\end{aligned}\quad (A10)$$

The characteristic and cooling synchrotron breaks and the maximum synchrotron flux become

$$\begin{aligned}\nu_m &= 7.72 \times 10^9 \text{ Hz} g^2(p) \left(\frac{1+z}{1.05} \right)^{\frac{k-2}{2}} \zeta_e^{-2} \varepsilon_{e,-1}^2 \varepsilon_{B,-3}^{\frac{1}{2}} A_{st}^{\frac{1}{2}} \beta_{-0.22}^{\frac{10-k}{2}} t_5^{-\frac{k}{2}}, \\ \nu_c &= 8.11 \times 10^{11} \text{ Hz} \left(\frac{1+z}{1.05} \right)^{\frac{2-3k}{2}} (1+Y)^{-2} \varepsilon_{B,-3}^{-\frac{3}{2}} A_{st}^{-\frac{3}{2}} \beta_{-0.22}^{\frac{3k-6}{2}} t_5^{\frac{3k-4}{2}}, \\ F_{\max} &= 7.01 \text{ mJy} \left(\frac{1+z}{1.05} \right)^{\frac{3k-4}{2}} \zeta_e \varepsilon_{B,-3}^{\frac{1}{2}} d_{z,26.78}^{-2} A_{st}^{\frac{3}{2}} \beta_{-0.22}^{\frac{8-3k}{2}} t_5^{\frac{3(2-k)}{2}}.\end{aligned}\quad (A11)$$

The synchrotron spectral breaks in the self-absorption regime can be expressed as

$$\begin{aligned}\nu_{a,1} &= 3.21 \times 10^{10} \text{ Hz} \left(\frac{1+z}{1.05} \right)^{\frac{4(k-2)}{5}} \zeta_e g(p)^{-1} \varepsilon_{e,-1}^{-1} \varepsilon_{B,-3}^{\frac{1}{5}} A_{st}^{\frac{4}{5}} \beta_{-0.22}^{-\frac{4k+5}{5}} t_5^{\frac{3-4k}{5}}, \\ \nu_{a,2}^{\text{syn}} &= 1.64 \times 10^{10} \text{ Hz} \left(\frac{1+z}{1.05} \right)^{\frac{(k-2)(p+6)}{2(p+4)}} \zeta_e^{-\frac{2(p-1)}{p+4}} g(p)^{\frac{2(p-1)}{p+4}} \varepsilon_{e,-1}^{\frac{2(p-1)}{p+4}} \varepsilon_{B,-3}^{\frac{p+2}{2(p+4)}} A_{st}^{\frac{p+6}{2(p+4)}} \beta_{-0.22}^{\frac{10p-kp-6k}{2(p+4)}} t_5^{\frac{4-kp-6k}{2(p+4)}}, \\ \nu_{a,3} &= 1.54 \times 10^{12} \text{ Hz} \left(\frac{1+z}{1.05} \right)^{\frac{9k-13}{5}} (1+Y) \varepsilon_{B,-3}^{\frac{6}{5}} A_{st}^{\frac{15-9k}{5}} t_5^{\frac{8-9k}{5}},\end{aligned}\quad (A12)$$

Table 1 shows the evolution of synchrotron light curves across the spectral and temporal indices, given the spectral breaks and maximum flux from eqs. A2 and A3. Also presented in Table 2 are the closure relations for each cooling condition seen during the coasting phase.

A2.0.2 Deceleration phase During the deceleration phase, the Lorentz factor of the lowest energy electrons and the one of those with energy above which they cool effectively are

$$\begin{aligned}\gamma_m &= 4.24 \times 10^1 \text{ Hz} \left(\frac{1+z}{1.05} \right)^{\frac{2(3-k)}{\alpha_s+5-k}} \zeta_e^{-1} g(p) \varepsilon_{e,-1} A_{st}^{-\frac{2}{\alpha_s+5-k}} \tilde{E}_{50}^{\frac{2}{\alpha_s+5-k}} t_6^{\frac{2(k-3)}{\alpha_s+5-k}}, \\ \gamma_c &= 1.01 \times 10^2 \text{ Hz} \left(\frac{1+z}{1.05} \right)^{-\frac{k+1+\alpha(k-1)}{\alpha_s+5-k}} (1+Y)^{-1} \varepsilon_{B,-3}^{-1} A_{st}^{-\frac{\alpha_s+3}{\alpha_s+5-k}} \tilde{E}_{50}^{\frac{k-2}{\alpha_s+5-k}} t_6^{\frac{k+1+\alpha_s(k-1)}{\alpha_s+5-k}}.\end{aligned}\quad (A13)$$

The characteristic and cooling synchrotron breaks and the maximum synchrotron flux become

$$\begin{aligned}\nu_m &= 1.68 \times 10^8 \text{ Hz} \left(\frac{1+z}{1.05} \right)^{\frac{20+k(\alpha_s-6)-2\alpha_s}{2(\alpha_s+5-k)}} \zeta_e^{-2} g(p)^2 \epsilon_{e,-1}^2 \epsilon_{B,-3}^{\frac{1}{2}} A_{st}^{\frac{\alpha_s-5}{2(\alpha_s+5-k)}} \tilde{E}_{50}^{\frac{10-k}{2(\alpha_s+5-k)}} t_6^{-\frac{30+k(\alpha_s-8)}{2(\alpha_s+5-k)}}, \\ \nu_c &= 6.48 \times 10^{11} \text{ Hz} \left(\frac{1+z}{1.05} \right)^{-\frac{8-2\alpha_s+k(3\alpha_s+2)}{2(\alpha_s+5-k)}} \epsilon_{e,-1}^{-\frac{3}{2}} (1+Y)^{-2} A_{st}^{-\frac{3(\alpha_s+3)}{2(\alpha_s+5-k)}} \tilde{E}_{50}^{\frac{3(k-2)}{2(\alpha_s+5-k)}} t_6^{\frac{k(4+3\alpha_s)-4\alpha_s-2}{2(\alpha_s+5-k)}}, \\ F_{\nu,\max} &= 5.2 \text{ mJy} \left(\frac{1+z}{1.05} \right)^{\frac{4+2k-4\alpha+3k\alpha_s}{2(\alpha_s+5-k)}} \zeta_e \epsilon_{B,-3}^{\frac{1}{2}} d_{z,26.78}^{-2} A_{st}^{\frac{3\alpha_s+7}{2(\alpha_s+5-k)}} \tilde{E}_{50}^{\frac{8-3k}{2(\alpha_s+5-k)}} t_6^{\frac{6-4k+6\alpha_s-3k\alpha_s}{2(\alpha_s+5-k)}}.\end{aligned}\quad (\text{A14})$$

In the self-absorption regime, the synchrotron break frequencies are

$$\begin{aligned}\nu_{a,1} &= 7.49 \times 10^9 \text{ Hz} \left(\frac{1+z}{1.05} \right)^{-\frac{55+8\alpha_s-k(21+4\alpha)}{5(\alpha_s+5-k)}} \zeta_e g(p)^{-1} \epsilon_{e,-1}^{-1} \epsilon_{B,-3}^{\frac{1}{5}} A_{st}^{\frac{25+4\alpha}{5(\alpha_s+5-k)}} \tilde{E}_{50}^{-\frac{4k+5}{5(\alpha_s+5-k)}} t_6^{\frac{3\alpha_s-16k+30-4k\alpha}{5(\alpha_s+5-k)}}, \\ \nu_{a,2} &= 1.52 \times 10^9 \text{ Hz} \left(\frac{1+z}{1.05} \right)^{-\frac{-2p(\alpha-10)+kp(\alpha_s-6)+6k(\alpha_s+4)-12(\alpha_s+5)}{2(p+4)(\alpha_s+5-k)}} \zeta_e^{-\frac{2(p-1)}{p+4}} g(p)^{\frac{2(p-1)}{p+4}} \epsilon_{e,-1}^{\frac{2(p-1)}{p+4}} A_{st}^{\frac{\alpha_s p+6\alpha-5p+30}{2(p+4)(\alpha_s+5-k)}} \epsilon_{B,-3}^{\frac{p+2}{2(p+4)}} \tilde{E}_{50}^{\frac{10p-kp-6k}{2(p+4)(\alpha_s+5-k)}}, \\ \nu_{a,3} &= 2.44 \times 10^9 \text{ Hz} \left(\frac{1+z}{1.05} \right)^{\frac{k(16+9\alpha_s)-13\alpha_s-20}{5(\alpha_s+5-k)}} (1+Y) \epsilon_{B,-3}^{\frac{6}{5}} A_{st}^{\frac{3(3\alpha+10)}{5(\alpha_s+5-k)}} \tilde{E}_{50}^{\frac{15-9k}{5(\alpha_s+5-k)}} t_6^{\frac{8\alpha_s-9k\alpha_s-11k-5}{5(\alpha_s+5-k)}}.\end{aligned}\quad (\text{A15})$$

Table 1 shows the evolution of synchrotron light curves across the spectral and temporal indices, given the spectral breaks and maximum flux from eqs. A5 and A6. Also presented in Table 2 are the closure relations for each cooling condition seen during the deceleration phase.

This paper has been typeset from a $\text{TeX}/\text{L}\text{\textit{a}}\text{TeX}$ file prepared by the author.